# Bimetallic Nanoparticles, Grown Under UHV on Insulators, Studied by Scanning Probe Microscopy

**Claude Henry and Clemens Barth**

**Abstract** Nowadays scanning probe microscopies (atomic force microscopy and scanning tunnelling microscopy) are common techniques to characterize at the atomic level the structure of surfaces. In the last years, these techniques have been applied to study the nucleation and growth of metal clusters (mono or bimetallic). Basic elements of scanning probe microscopy will be presented. With the help of the atomistic nucleation theory and using some earlier results obtained by TEM we show that the growth rate and the composition evolution of bimetallic particles grown from two atomic vapours sequentially or simultaneously condensed on insulating substrates (bulk or ultrathin film) can be predicted. The published work on the growth of bimetallic particles studied by STM and AFM is presented in a comprehensive way giving simple rules to select the best method to obtain homogeneous assemblies of nanoparticles with given mean sizes and chemical compositions. Although the application of scanning probes microscopy to the growth of supported bimetallic particles is relatively young, recent development of AFM and STM techniques paves the way for a complete in situ characterization, including morphology and surface composition.

C. Henry (✉) · C. Barth
CINaM-CNRS, Campus de Luminy, Case 913,
13288 Marseille cedex 09, France
e-mail: henry@cinam.univ-mrs.fr

C. Barth
e-mail: barth@cinam.univ-mrs.fr

D. Alloyeau et al. (eds.), *Nanoalloys*, Engineering Materials,
DOI: 10.1007/978-1-4471-4014-6_2, © Springer-Verlag London 2012

# 1 Introduction

In this chapter we will introduce scanning probe microscopy, which can be used to characterize supported bimetallic nanoparticles in situ. For sake of consistency we make the choice to restrict this overview on bimetallic particles supported on bulk insulators (alkali halides, oxides) or on ultrathin oxide films on metallic substrates. The choice of an insulator substrate has two main advantages: electronic decoupling of the particles from the substrate and tendency to grow 3D clusters instead of 2D islands. The nanoparticles are grown by atomic deposition under UHV whereas STM and AFM are best suited techniques to study in situ nucleation and growth of single bimetallic particles. The aim of the chapter is to provide a practical and comprehensive overview on the preparation and on the structural and morphological characterization of the nanoalloys. In the first section a rapid introduction of the scanning probes is presented with a selection of articles, reviews and textbooks for deeper understanding of these techniques. We also focus on new methods useful for the characterization of nanoparticles down to atomic scales. In the second section, an introduction of nucleation theory is presented restricted to the practical case considered here: nucleation and growth of bimetallic nanoparticles by condensing at room temperature (RT) or moderate temperature two metallic vapors, sequentially or simultaneously on an insulating substrate. In these conditions the atomistic nucleation theory is valid and re-evaporation of adatoms takes place (incomplete condensation). Analytic expressions are presented that will guide the reader in choosing the best conditions for the preparation of homogeneous collections of nanoparticles. In the third section we will review the main results on the characterization of the nucleation, growth, structure, morphology and chemical composition of the bimetallic nanoparticles by using STM and AFM together with some additional complementary techniques. From the different bimetallic systems investigated we will try to rationalize the results in term of empirical rules and analytical results from nucleation theory.

# 2 Introduction to Scanning Probes Microscopies: STM and AFM

In this section the scanning tunneling microscopy (STM) and atomic force microscopy (AFM) are first briefly reviewed (Sects. 1 and 2). Section 3 concentrates on the application of both techniques for studying the shape of supported metal clusters whereas the following section (Sect. 4) discusses the application of Kelvin probe force microscopy (KPFM). The aim of these four sections is to introduce the reader into the domain of STM, AFM and KPFM and to supply the reader with reviewing literature, which can be used for a further, deeper reading.

## 2.1 Scanning Tunneling Microscopy

The introduction of scanning tunneling microscopy (STM) by Binning, Rohrer, Gerber and Weibel in 1982 [1] revolutionized experimental studies of conducting surfaces in many scientific fields, ranging from physics to chemistry and up to biology. This specific local imaging technique has been reviewed several times [2–4] and is also described from the theory point of view [5, 6]. The reader is referred to two well-known text books [7, 8], which discuss all aspects of the technique, whereas a brief overview is given in the following.

The principle of a scanning tunneling microscope is quite simple: If the surfaces of two metallic electrodes (tip and surface) are brought very close together, *e.g.* to a distance of about one nanometer and less, electrons can overpass the gap distance and *tunnel* from one conductor to the other one, which is thanks to the quantum mechanical tunneling probability [7]. The tunneling is done such that the electrons tunnel from the metal with the higher Fermi level to the other metal with the lower Fermi level. In order to create a difference of Fermi levels, a so-called *bias potential* is applied in STM between the two conductors (Fig. 1a). The innovative idea of Binnig and Rohrer was to shrink one of the surfaces to an atomic size such that the initial surface becomes a very sharp object called 'tip', which apex is formed by only a few atoms. With help of piezo-electric motors, the surface is scanned in X and Y directions and the flow of electrons (tunnel current) is kept constant by adjusting the tip-surface distance upon changes in the surface topography during scanning. The relative changes in the tip-surface distance are recorded in dependence on X and Y so that an image of the surface is created. Because the tip apex is formed by few atoms only and because the tunnel current depends exponentially on the tip-surface distance, it is almost the last atom of the tip that produces the contrast of STM images. In best cases, the true atomic resolution can be obtained (Fig. 1b). Note that apart from the latter *topography imaging mode*, a second mode exists: In the *constant height mode* the tip keeps a constant distance to the surface during scanning (see scanning mode explained in Ref. [7]) such that it does not follow the topography. Because of the varying topography and because the tip follows only the mean inclination of the sample, the tunnel current is varying during scanning and is recorded in dependence on X and Y such that the resulting *tunnel current image* contains all information of the surface. The constant height mode can be used only on flat surfaces but permits scanning surfaces with high speed even at video frequencies (see example in Ref. [9]).

STM has become the standard surface analysis technique in surface science, especially in surface physics and surface chemistry. Applications have shown true atomic resolution first on semiconductor surfaces [1] and later on a metal surfaces [12]. In the case of surfaces of metallic alloys the chemical identification of atoms is difficult because STM has in general no specific chemical sensitivity. However in some circumstances atomically resolved images can present a chemical sensitivity as it was first shown by Varga's group (see Fig. 2b) in 1993 on $Pd_{25}Ni_{75}(111)$ [13]. Later, the same group has succeeded in imaging chemical

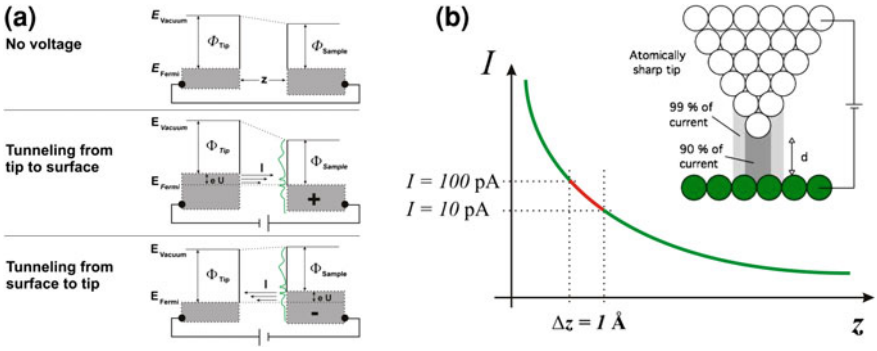


**Fig. 1** The principle of STM. **a** The Fermi levels of two electrodes (tip and surface) are aligned if they are connected from behind. If the tip and surface are separated by a distance of $z \approx 1$ nm and if a potential $U$ is applied between both electrodes, electrons tunnel from the electrode with the higher Fermi level ($E_{Fermi}$) to the other one with the lower Fermi level. If the tip is at positive potential in the case here, the electrons tunnel from the sample to the tip and vice versa. **b** The electron flow (tunnel current I) depends exponentially on the tip-surface distance $z$. A change of the distance by $\Delta z = 1$ Å changes the tunnel current by one order of magnitude. This is the reason why the tip can be precisely positioned with picometer precision above the surface. It also explains that it is almost the last atom of the tip that contributes to the image contrast. Because of the small dimension of the atom, atomic resolution can be obtained

atomic contrast in several surfaces of bulk metallic alloys like PtRh [11, 14], AgPd [15], CoPt [16], FeNi [17]. Other groups have imaged with a chemical contrast alloyed surfaces obtained by depositing a thin layer of a metal on the surface of another metal like in the case of CuPd [18, 19]. Ultrathin films of insulators supported on metal single crystals can also be imaged at atomic resolution by STM like NaCl/Cu [20], MgO/Ag [21], alumina/NiAl [22]. Chemical reactions on metal surfaces can be followed at atomic scale by STM [23], even at high-speed, which permits to produce movies of surface reactions [9]. Not only imaging can be done but also spectroscopy, which has become a large field in STM. Different spectroscopy modes exist like STS (scanning tunneling spectroscopy), constant current spectroscopy (CCS), constant separation spectroscopy (CSS) (see overview in Refs. [7, 8]). During a spectroscopy experiment the tip either scans the surface or is hold at one position above the surface. In STS, when the tip is hold at one point on the surface, the bias voltage V is swept and the tunnel current I recorded so that I(V) curves are obtained, which are mostly converted to $dI/dV$ or $dI/dV/(I/V)$ curves. The latter two types of curves are a fingerprint for the local density of states (LDOS) at the Fermi level for the specific position on the surface. It helps to study the local electronic structure of the surface. More recently a new type of measurement which is like inelastic electron tunneling spectroscopy (IETS) but acquired with an STM is able to resolve vibration of an adsorbed isolated molecule on a surface [24]. In this case one records the second derivative of the current ($d^2I/dV^2$) as a function of the bias voltage. Vibrational/rotational modes of a single molecule can be excited for instance and electron induced modifications of

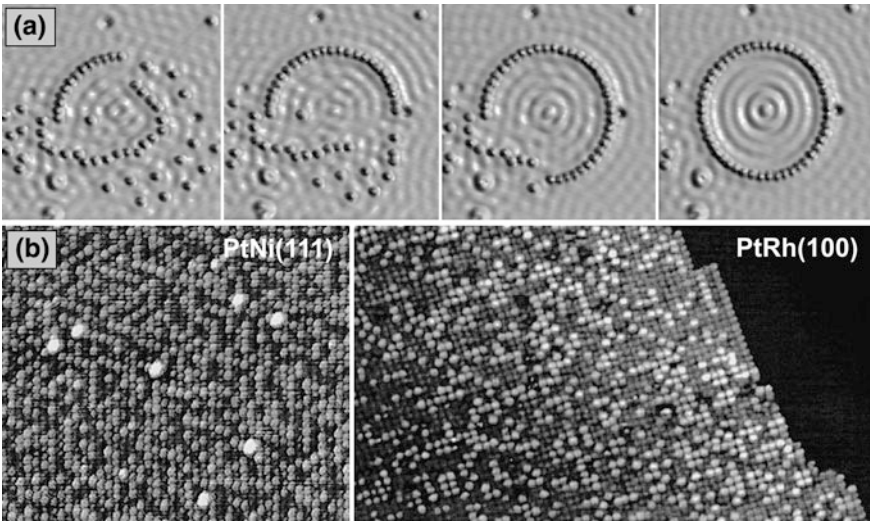


**Fig. 2** **a** Series of STM images which were obtained in between several steps of atom manipulation. Thanks to the manipulation, 48 Fe ad-atoms could be placed into a circle on a crystalline Cu(111) surface at 4 K (from Ref. [10], reprinted with permission from AAAS and Copyright (1993) IBM). **b** Surfaces of metal alloys. In the NiPt case a *chemical* contrast can be seen, well-separating the two types of atoms. However, the contrast strongly depends on the tip composition (last tip atom). On PtRh(100) a chemical contrast can be always observed. The bright atoms are the Rh atoms whereas the dark ones are the Pt atoms (from Ref. [11], copyright (1999), with permission from Elsevier)

molecules (desorption, dissociation, hopping, chemical reactions) can be realized. In order to position the tip and its last atoms with utmost precision above single surface atoms or molecules, tunneling spectroscopy is mostly applied at liquid nitrogen or helium temperatures where the tip's last atom remains for a very long time of days above a single molecule for instance.

A breakthrough in STM was certainly the work of Eigler and Schweizer [25] who demonstrated for the first time that single Xe atoms adsorbed on a Ni surface can be manipulated such that they are moved on the surface by the STM tip. The most impressive example is the arrangement of 48 Fe ad-atoms in a circle on a Cu surface which represents a quantum corral where the confinement of electrons produced standing waves [10] (Fig. 2a). Manipulation of molecules can be used to functionalize the apex of the STM tip. It has been shown that the presence of a CO molecule can improve the topographic resolution in the STM image but it can also resolve vibrational modes in adsorbed molecules that are not visible with a bare tip [26]. Bimetallic AuPd atomic chains have been fabricated by atom manipulation on a metal substrate and STS has shown the evolution of the electronic structure by adding Pd atoms in a gold chain [27]. In combination with scanning tunneling spectroscopy (STS), the nano-manipulation has been used especially in surface chemistry for inducing chemical reactions by the tip like inducing an 'Ullmann' reaction [28] or controlling the hydrogenation of a single molecule [29].

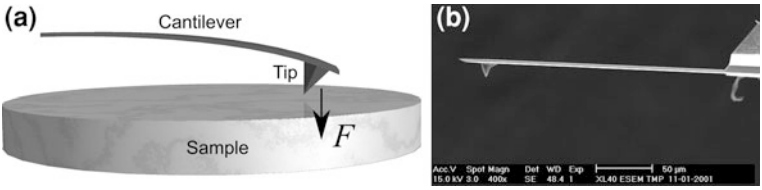


**Fig. 3** The principle of AFM. **a** A pyramidal tip is attached to a beam, the *cantilever*. As soon as the tip is close to the surface ($z < 5$ nm) a force acts onto the apex of the tip attracting the tip and cantilever towards the surface. The result is that the cantilever bends, what can be measured by optical laser methods for instance. **b** A cantilever-tip system is nowadays produced from one single silicon or silicon nitride crystal by etching methods. Cantilevers with almost all possible characteristics (size, resonance frequency, coating etc.) are commercially available today

## *2.2 Atomic Force Microscopy (Scanning Force Microscopy)*

Many important materials are insulators, which surfaces cannot be imaged with the STM. This concerns especially oxide materials like bulk $Al_2O_3$ or MgO, which surfaces are used to support metal clusters in catalysis for instance. This limitation has been soon realized after the introduction of the STM, and four years later, in 1986, Binnig, Quate and Gerber invented a second type of microscope, the atomic force microscope (AFM) [30]. The AFM allows nowadays obtaining almost the same type of resolution on almost any atomically flat and clean surface, even if the material is an insulator [31].

The principle of the AFM is somewhat similar to the one of the STM on the one hand but quite different on the other. Like in STM a sharp tip is used, which is, however, attached in perpendicular position at one end of a flexible beam called *cantilever* (Fig. 3). The other end of the cantilvever is fixed. If the tip is brought into a close distance to the surface ($z < 5$ nm), a force can be detected between tip and surface by measuring the bending of the cantilever. If the force is kept constant during scanning such that variations of the surface topography are compensated by adjusting the tip-surface distance by a regulation loop, an image is obtained representing the topography of the surface. In this *contact AFM mode* (c-AFM), the very end of the tip is always in hard contact with the surface due to the *jump-into-contact* mechanism (see Ref. [32] for further details). It has been shown that in this *static mode* the AFM cannot yield a high resolution at the atomic scale because the last tip atoms modify or even change the atoms of especially reactive surfaces [33, 34]. In 1991, the so-called *frequency modulated non-contact AFM mode* (FM nc-AFM or just nc-AFM) was introduced by Albrecht, Grütter, Horne and Rugar in order to overpass the limits of the c-AFM [35]. In FM nc-AFM, the cantilever and tip are excited to oscillation at their resonance frequency $f_0$. As soon as a force acts onto the tip, the resonance frequency changes (detunes) to a value f, and the tip-surface distance is adjusted upon changes which appear in the detuning $\Delta f = f - f_0$ during scanning the surface. The detuning $\Delta f$ is therefore the same type of regulation signal as it is the force in c-AFM or the tunnel current in STM.

In nc-AFM, the tip's last atoms can be brought very close to the surface in a distance of some Angströms, at which the true atomic resolution is mostly obtained [36]. Although the atomic contrast formation in nc-AFM is different with respect to STM, one can roughly state that also in nc-AFM the last atoms of the tip apex produce the atomic contrast. Starting with the first-time atomic resolution in 1995 on Si(111)7 × 7 [37], it has been impressively shown in the last 15 years that the true atomic resolution can be obtained on any atomically flat and clean surface, independently if it is the surfaces of metals, alloys, semi-conductors, insulators or oxides (many applications are reviewed in Refs. [31, 38–41]). The nc-AFM catches successively up with its sister technique STM, which can be best seen by recent manipulation experiments in nc-AFM where single atoms and molecules could have been moved on the surface [36]. As in STM, spectroscopy exists also in nc-AFM, which is based on recording and interpreting the detuning and, with it, the force or potential in dependence on the tip-surface distance or even additionally on X and Y (3D force fields). In combination with theory, force spectroscopy is mostly used to identify single atoms on surfaces as it has been shown on Sn and Pb covered Si(111) surface [42, 43] (see Fig. 4a). In some cases an identification can be done also on real insulator surfaces by just imaging as impressively demonstrated for $CaF_2$(111) [44] or on the (001) surfaces of $CdCl_2$ or $MgCl_2$ doped NaCl [45] (see Fig. 4b). In all such experiments, the chemical contrast in images with atomic resolution strongly depends on the nature of the tip's last atoms.

## *2.3 Imaging the Shape of Metal Clusters with the STM and AFM*

Most importantly for this chapter is the contribution of STM and AFM in the in situ imaging of the morphology of metal clusters supported on non-metallic substrates (see Ref. [46] for a review on the subject). Figure 5 presents Pd nanoparticles grown on $MoS_2$(0001), (ex situ) TEM and (in situ) STM images of the same sample are displayed in (a) and (b), respectively [47]. On the STM image the particles appears larger and the edges are rounded in comparison with the TEM image. The size distributions (Fig. 5c) from the two images indeed show an increase of the mean size in STM (14 against 12 nm by TEM). This enlargement in the STM images of 3D objects is typical and due to a deformation of the shape of the object by the scanning tip. This effect is schematically represented in Fig. 6. The imaged profile is enlarged by an amount which depends on the shape of the tip and on the slope of the facets: steeper is the facet smaller is the deformation. If the exact shape of the tip is known the original profile of the particle can be restored but with a loss of information at the bottom as seen on Fig. 6 (for example re-entrant angles cannot be imaged).

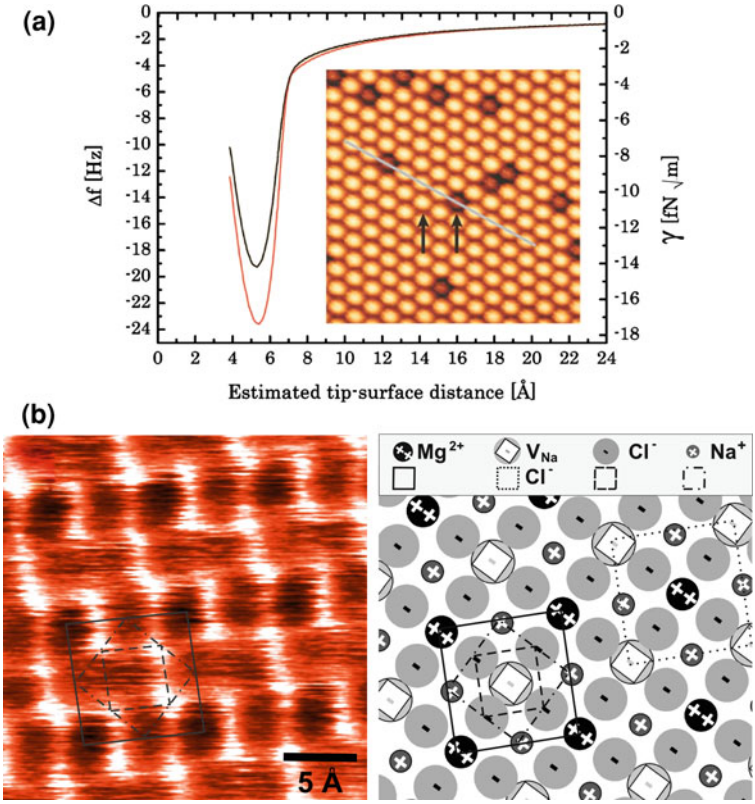


**Fig. 4** **a** High resolution nc-AFM image of Sn on the Si(111) surface and set of force curves measured over Sn (*bright*) and Si (*dark*) atoms. Both type of atoms produce a clear chemical contrast in the image but also in the detuning (Δf) versus distance curves, which represent the tip-atom interaction (from Ref. [43], copyright (2006) by The American Physical Society). **b** Noncontact AFM images obtained on the (001) surface of a $Cd^{2+}$ doped NaCl crystal. Thanks to the specific geometric structure of each sub-lattice formed by the $Na^{+}$, $Cl^{-}$, $Cd^{2+}$ ions and the chemical contrast each ion is producing, all ionic species can be unambiguously identified (see left drawing) by just imaging (from Ref. [45], copyright (2008) by The American Physical Society)

The top facet is not distorted and if it is large enough and flat, atomic resolution can be obtained in STM as seen on Fig. 7b for a Pd nanoparticle on an ultrathin film of alumina on NiAl(110) [48] or for Pt nanoparticles on $TiO_2$(110) [49]. If the particles are prepared at high temperature they can then get the equilibrium shape which is defined by the Wulff theorem for a free particle and the Wulff–Kaichew theorem from a supported one [46]. From a precise measurement of the particle height and of the top facet size, it is possible to deduce the adhesion energy of the particle [46, 48, 50].

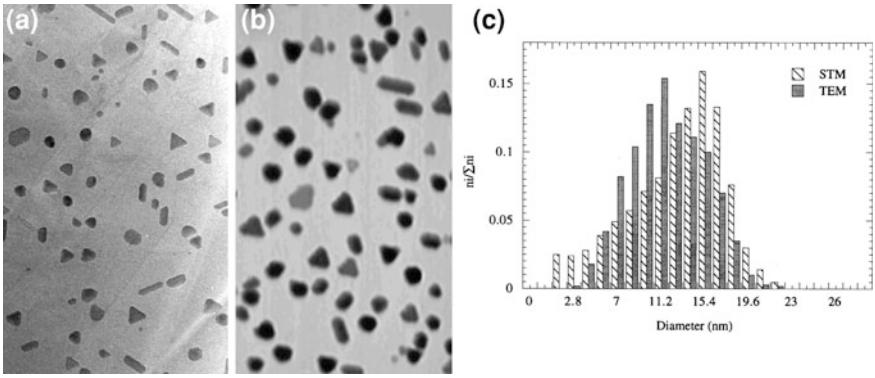


**Fig. 5** TEM (**a**), STM (**b**) and corresponding size distributions (**c**) for Pd nanoparticles grown on $MoS_2$(0001) under UHV. The STM images are recorded in situ after the deposition while TEM pictures are obtained ex situ after thinning of the sample by exfoliation. From Ref. [47], copyright (2000), with permission from Elsevier

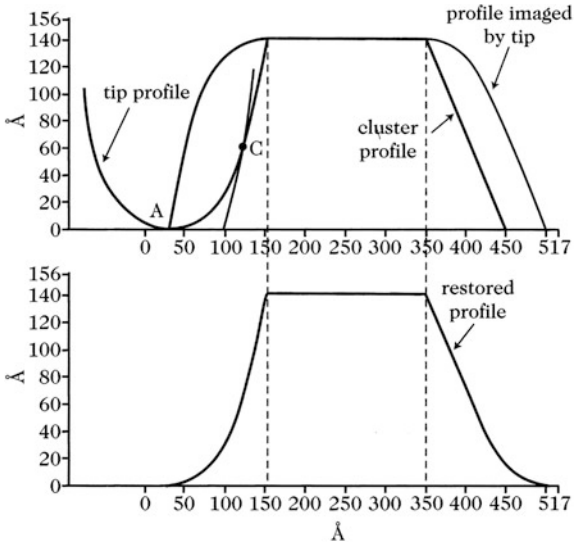


**Fig. 6** Profile view of the deformation of the image of a 3D particle due to the shape of the scanning tip. From Ref. [46], copyright (2005), with permission from Elsevier

In the case of tiny clusters it has been possible to image at atomic resolution all the atoms on the surface of metal clusters [51]. Figure 7a shows an STM image of a Pd clusters on $MoS_2$(0001) containing exactly 27 atoms (20 in the first layer and 7 in the second one) [51]. The top layer (sulphur atoms) of the substrate is also imaged at atomic resolution then the epitaxial orientation of the metal clusters can be revealed. The sulphur atoms at the periphery of the clusters appear higher probably through an electronic effect. Unfortunately such nice atomically resolved images of metal clusters are scarce because they need to have a very flat sample and an exceptional tip (the control of the tip in STM experiments is still a major issue).

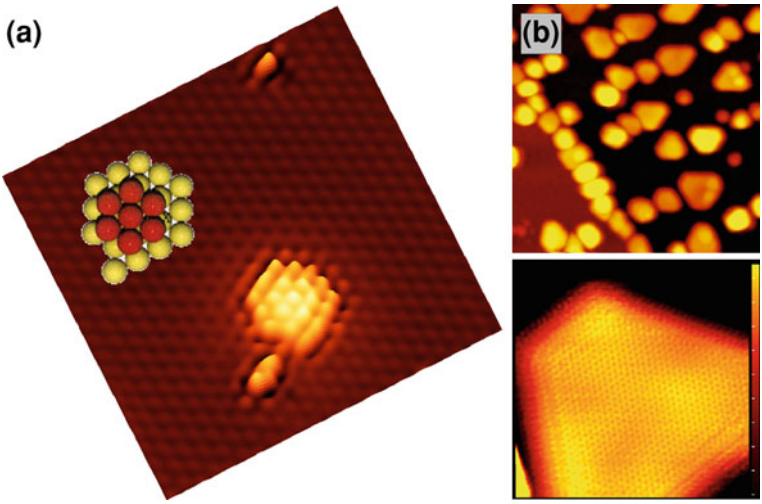


**Fig. 7** STM images of Pd clusters showing atomic resolution. **a** Pd cluster on $MoS_2$(0001) containing 27 atoms, a ball model (inset) shows the atomic arrangement of the atoms in the two layers (from Ref. [51], copyright (1997), with permission from Elsevier). **b** Palladium nanoparticles (5 nm) on a thin $Al_2O_3$ film supported on NiAl(110) showing atomic resolution on the top (111) facet (image at the bottom) (from Ref. [48], copyright (1999) by The American Physical Society)

In the case of imaging the shape of nanoparticles by AFM the problem of the deformation of the image by the tip shape is still present and even worth because commercial AFM tip are generally bigger than STM tips (see Ref. [46]). A solution to reduce this effect is to grow a nanotip at the apex of the AFM tip in a SEM or a FIB [46] or even to glue a carbon nanotube [52]. Contact AFM has been very often used to image nanoparticles supported on insulators but the large majority of these studies were performed in air. Some studies on the growth of metal nanoparticles have been performed in situ under UHV (*e.g.* Au/mica [53], Au/MgO [54]). In the case of large Au particles (around 10 nm) on mica (001), the atomic lattice of the top (111) facet has been imaged [53] but in contact mode the true atomic resolution cannot be obtained, that means that point defects cannot be imaged.

Almost as soon as the technique became available, nc-AFM has also been applied in studies of various adsorbed nanoclusters on different substrate surfaces as reviewed in Ref. [41]. One of the main aims in nc-AFM is to provide high resolution of both the cluster and the surface and to obtain atomic scale details of the clusters and adsorption sites. Efforts in this direction have generally focused on standard model systems, particularly Au nanoclusters on alkali halide surfaces [55, 57]. These studies often provided atomic resolution on the substrate. However, approaching closer to a nanocluster resolves it only as a fuzzy hemisphere (Fig. 8a) [55], rather than as its true geometric shape. However on

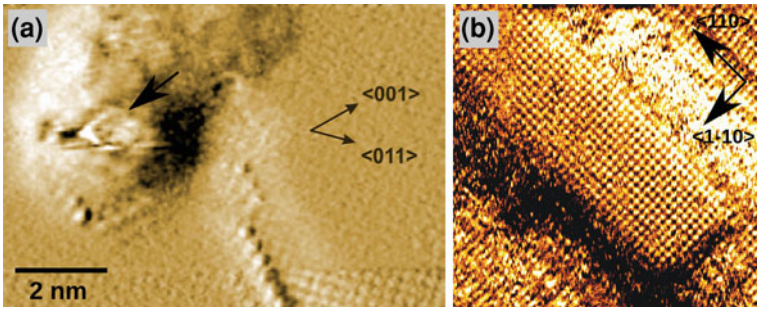


**Fig. 8** Noncontact AFM images of supported gold particles. **a** Detuning image of a 2 nm gold cluster on KBr(001), the cluster appears like a fuzzy cloud while the top rectangular facet can bee seen. The KBr substrate is imaged at atomic resolution (from Ref. [55]). **b** Gold nanoribbon on InSb(001). The top facet is imaged at atomic resolution (from Ref. [56])

large gold ribbons supported on InSb(001) particles atomic resolution has been obtained [56] (Fig. 8b). The fuzzy shape of the 2 nm cluster in Fig. 8a is in fact the image of the apex of tip which appears at several places on large scale images [55]. This is another effect of the deformation of the image of small objects by the shape of the imaging tip [55, 58]. In the extreme case where the tip is much larger than the cluster, the cluster is rather a 'needle' and images in fact the tip apex (Fig. 8a). In such a case, the same type of tip-image can be observed at all clusters on the surface, which leads to very complex patterns if the cluster density is high (Fig. 9b).

Significant improvement in imaging the shape of nanoparticle by nc-AFM can be achieved by imaging the surface in the constant height mode as recently demonstrated [59]. In this specific mode the tip scans the surface in a constant height and only the very last nanometer of the tip is put into a close distance to the top facets of the clusters. Since the tip does not follow anymore the contours of the clusters the convolution is greatly reduced. An extensive experimental and theoretical study of Pd nanoclusters on MgO showed that the real shape of the clusters which is a square pyramid truncated on the top by a (001) facet [46] could be seen in constant height mode independently of the shape of the tip [60] (compare image (b) in Fig. 9 with image (c) of same clusters and with the TEM image (a)).

## *2.4 Kelvin Probe Force Microscopy in nc-AFM*

A severe limitation for all scanning probe microscopy techniques is the lack of chemical sensitivity; one can rarely determine the chemical nature of surface atoms or supported molecules or clusters from imaging the surface topography alone (except in some peculiar circumstances where chemically resolved atomic

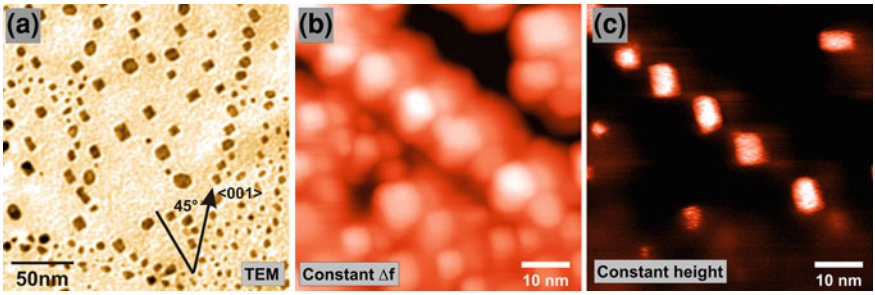


**Fig. 9** Pd clusters (7 nm) on MgO(100) imaged in situ by noncontact AFM and ex situ by TEM. **a** TEM image obtained using the carbon replica transfer method. The clusters have the shape of a square pyramid and a mean size of 7 nm (from Ref. [46], copyright (2005), with permission from Elsevier). **b** Nc-AFM topography image obtained in the constant $\Delta f$ mode. **c** Constant height image representing the detuning $\Delta f$ of the same Pd clusters. The topography image shows a typical contrast, which was strongly influenced by the tip. However, the convolution could be reduced by imaging the clusters in the constant height mode (from Ref. [60], copyright (2008), American Institut of Physics)

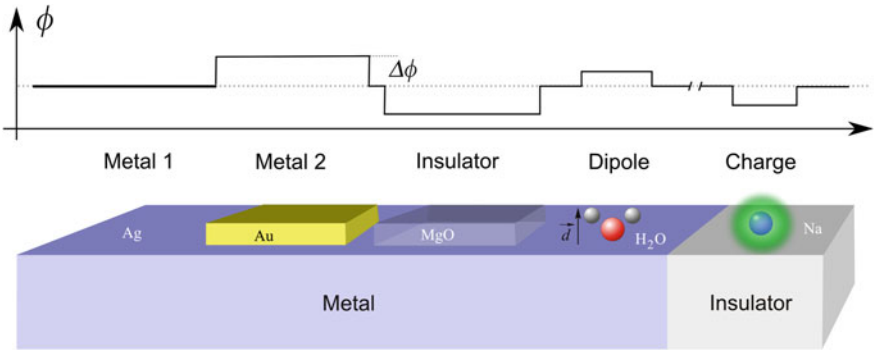


**Fig. 10** Objects of different chemical compositions exhibit differences in the local work function on the surface (metal) or in the electrostatic surface potential (insulators), which can be used for the chemical identification in AFM. From Ref. [41]

contrast can be obtained *e.g.* Figs. 2b and 4a). However, in AFM the long-range electrostatic forces alone may assist chemical identification. As illustrated in Fig. 10, nano-objects of different chemical composition (metal or insulating films, ions, molecules, etc.) change the local electrostatic surface potential by changing the local work function (WF) of a metal surface [61–63]. Such objects also change the local electrostatic potential when supported on an insulating surface [64]. Measuring the local work function or electrostatic potential of a surface by AFM with a resolution in the mV range and at the nanometer scale can indeed be used for chemical identification of surface species. Apart from other electrostatic AFMs like Electrostatic Force Microscopy (see Refs. [65–67]), this can be especially

achieved using Kelvin probe force microscopy (KPFM), which has become a well-established surface science tool in many scientific disciplines [41]. For a detailed description of KPFM the reader is referred to some papers [41, 68–70] whereas the principle of the KPFM is briefly summarized in the following.

In a KPFM measurement, a *dc* ($U_{dc}$) and an *ac* voltage ($U_{ac}$) with frequency $f_{ac}$ are applied between tip and surface. Owing to the modulation of the electrostatic force by the *ac* voltage, the electrostatic contribution, oscillating at frequency $f_{ac}$ and also at 2 $f_{ac}$, can be extracted (first and second harmonic) by a Lock-In amplifier, which is supplying the ac voltage at the same time. The first harmonic includes a term with $U_{dc} + U_{CPD}$, where the potential difference $U_{CPD}$ is the contact potential difference for conducting tip-surface systems. By varying the dc voltage such that the first harmonic becomes zero ($U_{dc} = -U_{CPD}$), the total electrostatic tip-surface interaction is minimized at each point on the surface and a so-called *Kelvin image* of $U_{dc} = -U_{CPD}$ is obtained. The contact potential difference $U_{CPD}$ is in fact proportional to the difference of WF between tip and surface ($U_{CPD} * \mathrm{e} = \phi_{Surface} - \phi_{tip}$). If at two different places on the surface the contact potential difference $\mathrm{U_{CPD}}$ is obtained, the difference of the potentials, $U_{CPD,\ 1} - U_{CPD,\ 2}$, is proportional to the WF difference of the materials at the two places (($U_{CPD,\ 1} - U_{CPD,\ 2}$) * $\mathrm{e} = \phi_{Surface,\ 1} - \phi_{Surface,\ 2}$). In other words, the contrast of Kelvin images ($U_{dc} = -U_{CPD}$) reflect variations of the surface WF. Since surface charges or dipoles can significantly change the condition $U_{dc} = -U_{CPD}$, Kelvin images represent also the distribution of surface charges and dipoles, which is especially the source of contrast in Kelvin images obtained on bulk insulator surfaces [71, 72].

A major goal for KPFM is to characterize supported metal clusters on surfaces. Metal nanoclusters on oxide surfaces for instance play a particularly important role in heterogeneous catalysis [73, 74] then it is particularly interesting to obtain information on the electronic structure of an individual clusters (local work function, charge state…). Quite often the support can change the electronic and therefore the catalytic properties of the clusters [74]. Since phenomena like charge transfer or polarization modifies the electronic properties (WF of large clusters), KPFM is a promising technique for studying all this with nanometer resolution.

Simple surface systems, demonstrating that KPFM works quite efficiently, are conducting surface systems (*e.g.* metal clusters on graphite or on low bandgap semiconductors) [75–77]. KPFM accurately represents the work function differences between large clusters and the substrate surface with a nanometer resolution and with an energy resolution in the mV range as shown for gold clusters on HOPG [75], Si [76] or InSb [77]. With respect to bulk insulators support, KPFM has been mainly used to study metal clusters on alkali halides surfaces like NaCl(001) [78] or oxide surfaces like $TiO_2$(110) [79] or MgO(001) [80].

In such experiments, the bulk insulator separates the clusters from a conducting support (metallic sample holder), so that no conducting channels exist between the clusters and the support. This aspect is important especially when charge is transferred between a cluster and the tip during contact. The charge stays for a very long time on the cluster and electrons can be transferred only to the neighboring

clusters located at nanometer scale distances from the charged cluster [78]. When clusters are 'neutral' on the insulating surface, KPFM measures the WF difference between the insulator on the conducting sample holder and large clusters [79, 80]. However, in most cases, the clusters are influenced by the insulating support, which can be observed for gold clusters on alkali halide surfaces [78], palladium clusters on MgO(001) [80] or even for single platinum atoms on the $TiO_2$(110) surface [81]. Important issues in KPFM are the lateral resolution, the accuracy of WF measurements and the resolution in voltage. Because KPFM is detecting only the electrostatic tip-surface interaction, the lateral resolution and accuracy of a measurement depend much more on the tip size and shape than it is the case in the standard topography imaging mode. The reason is that electrostatic forces are much more long-ranging (under specific conditions up to 50 nm and more) than forces like van der Waals and short-ranges forces, which are responsible for the topography contrast. If electrostatic forces are more long-ranging, they act on a larger tip volume and, as a consequence, the convolution with the tip is increased. These aspects have been studied in particular on ultra-thin insulating films supported on metal surfaces. These surfaces are well suited for such studies since the films lower the WF of the metal underneath by more than 0.5 eV and the surface is quite flat. As a rule of thumb it can be said that although a lateral resolution of some nanometer can be obtained on such flat surfaces the accuracy is mostly relatively low. Several 10 nm large structures are needed such that the WF is enough saturating. However, since it may happen that the tip may change due to, *e.g.*, tip-changes during scanning, the tip can reduce the size of its apex or so-called nanotips are formed at the tip apex. This greatly enhances the lateral resolution but also the accuracy of KPFM measurements [82]. The lateral resolution and accuracy increase as soon as nanometer large nano-objects like clusters are imaged. The reason is that when the tip is placed above a cluster, which has a height of some nanometers for instance, the tip does not 'feel' anymore contributions of the substrate surface. Lateral resolutions of a few nanometer can be obtained in best cases (Fig. 11).

# 3 Nucleation and Growth of Bimetallic Clusters on Insulators

## *3.1 Overview of Nucleation and Growth Theory*

### 3.1.1 Nucleation Kinetics

Nucleation theory has been strongly developed in the 1960/1970 s in particular to understand the early stages of deposition of metallic thin films on insulators which were also used as model for epitaxial growth [83–85]. Classical nucleation theory was originally developed by Volmer [86]. From this theory a nucleus can spontaneously grow if it has a critical size $i^*$. Taking the case of a liquid droplet the radius of the critical nucleus is:

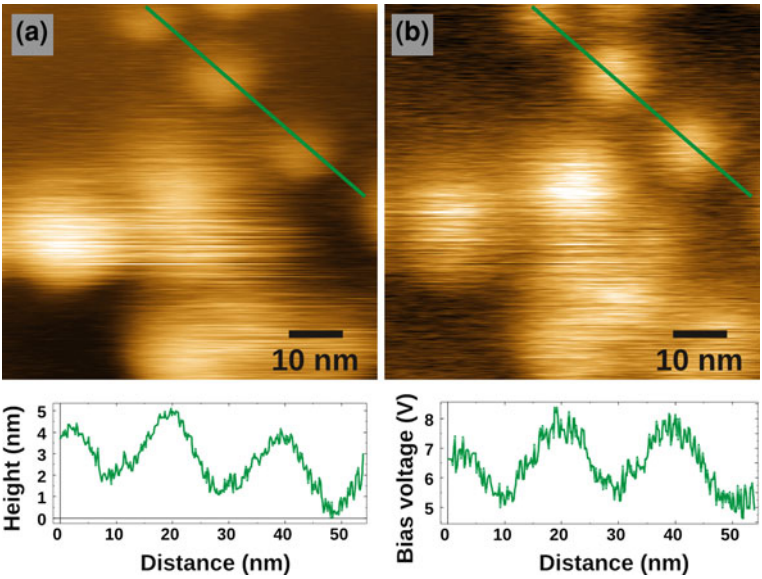


**Fig. 11** Pd clusters grown on MgO(001): **a** topography, **b** Kelvin image. The line profile at bottom shows that the lateral resolution in the Kelvin mode is at least 5 nm. The mean value of the difference of contact potential between Pd cluster and MgO is 2.4 V which corresponds to the difference of work function of bulk materials. From Ref. [80], Copyright (2009) American Chemical Society

$$R^* = 2\gamma v/\Delta\mu \tag{1}$$

$\gamma$ is the surface energy of the droplet, $v$ is the atomic volume and $\Delta\mu$ is the variation of the chemical potential between gas and liquid phases which is expressed by:

$$\Delta\mu = kT\ln(P/P_\infty) \tag{2}$$

$P/P_\infty$ is the supersaturation, $P$ and $P_\infty$ are the actual vapour pressure around the nucleus and of the infinite liquid phase, respectively. The nucleation rate is expressed by:

$$J = C\exp(-\Delta G^*/kT) \tag{3}$$

$\Delta G^*$ is the energy barrier (nucleation barrier) to form the critical nucleus and $C$ is a constant.

However in the case of condensation of a metal vapour on an insulator substrate the supersaturation can be very high. Taking as an example the condensation of Pd on an MgO crystal at 700 K the supersaturation is around $10^{12}$ then from Eq. (1) the critical radius would be 0.17 nm. Thus in this case the critical nucleus is only one atom, which means that the dimer is already stable. In that case the classical nucleation theory is no longer available. The growth process occurs by accretion of

adatoms (like a polymerization process). It is described by the so called 'atomistic nucleation theory' which has been developed by Zinsmeister [87] from basic ideas first expressed by Frenkel [88]. The rate equations given by Zinsmeister express the variation with time of the number of clusters of size $i$:

$$dn_i/dt = \omega_{i-1}n_{i-1} - \omega_i n_i \quad \text{for } i = 2, 3 \ldots \infty \tag{4}$$

$\omega_i$ is the attachment frequency of an adatom to a cluster containing i atoms which is expressed by:

$$\omega_i = \sigma_i D n_i \tag{5}$$

where $D$ is the diffusion coefficient of an adatom and $\sigma_i$ is the capture number for a cluster of size i.

To calculate the number of nuclei present on the substrate we have to integrate the system of differential equations which can reduced in only two equations [87] which can be solved numerically if we know the various capture numbers. For sake of simplicity Zinsmeister assumes that it is a constant (between 1 and 4). From this scheme the nucleation frequency is:

$$J = 2\omega_1 n_1 \tag{6}$$

Assuming that the growth is negligible the density of adatoms is equal to the stationary value:

$$n_1 = F\tau \tag{7}$$

where $F$ is the flux of atoms impinging on the substrate and $\tau$ the life time of an adatom before desorption. Then combining Eqs. (5)–(7) the nucleation rate becomes:

$$J = 2\sigma_1 D F^2 \tau^2 \tag{8}$$

Then the nucleation rate is proportional to the square of the impinging flux for a homogeneous substrate without defects.

The diffusion coefficient is expressed by:

$$D = (va^2/4)\exp(-E_d/kT) \tag{9}$$

The life time t is expressed by:

$$\tau = (1/v)\exp(E_a/kT) \tag{10}$$

where $v$ is the frequency factor, $E_a$ and $E_d$ are the adsorption energy and diffusion energies of an adatom. Combining Eqs. (8)–(10) the nucleation frequency becomes:

$$J = (\sigma a^2 F^2/2v)\exp[2E_a - E_d)/kT] \tag{11}$$

Generally insulating surfaces (like alkali halides, oxides) contain point defects which strongly bind adatoms. If an adatom is indefinitely trapped on a defect it is already a stable nucleus, then the critical size is $i^* = 0$. This case is called nucleation on defects. Robins and Rhodin have treated this case and compared with TEM measurements of the nucleation of Au on MgO(100) [89]. The nucleation rate is now expressed by:

$$J = \sigma D n_1 n_o \tag{12}$$

where $n_o$ is the density of defects. Again assuming a negligible growth the nucleation frequency becomes:

$$J = (\sigma a^2 F/4) \exp[(E_a - E_d)/kT] \tag{13}$$

Now the nucleation rate varies linearly with the flux, this dependency allows the separation between nucleation on perfect surface and nucleation on point defects. This linear dependency has been experimentally observed for Au/MgO [89], Pd/MgO [90]. In that simple case the rate equations can be integrated (still assuming a negligible growth) and the density of clusters as a function of time reaches exponentially the density of defects [89]:

$$n(t) = n_o[1 - \exp(-tJ/n_o)] \tag{14}$$

This exponential behaviour has been observed for Au and Pd nanoparticles on MgO [89, 91] and also for Pd/NaCl and CuPd/NaCl [92]. However, contrary to this simple theory of nucleation on defects, the saturation density of clusters has been observed to decrease by increasing temperature for Au/MgO (in situ AFM study) [54], Pd/MgO studied in situ by AFM [93] and by He diffraction [91]. In fact, the assumption that defects are perfect sinks for adatoms is not true, due to the finite adsorption energy on a defect site, at high temperature adatoms can escape from the defects and the number of populated defect sites decreases with increasing temperature. This effect has been included in a more accurate treatment of point defect nucleation made by Venables and coworkers [93, 94] which has been compared with the AFM study of the nucleation of Pd/MgO [93]. From this model, the saturation density of clusters is equal to the density of defects only on a limited range of temperature, at high temperature the density of clusters decreases but also at low temperature the cluster density is larger due to the fact that nucleation on normal sites is no longer negligible (Fig. 13).

### 3.1.2 Growth Kinetics

By integration of the system of rate Eq. (4) one obtains the size distribution of the growing clusters at each time. Zinsmeister has solved this system of differential equation assuming a constant value for the attachment frequency ($\omega_i$) [95]. However by this treatment several aspects of the growth of clusters are not taken into account: the direct impingement on the growing cluster (which is important at

the late stages of growth) and the competition between clusters for the capture of diffusing adatoms (which is important at high density of clusters). Several authors have tried to treat more accurately the calculation of the attachment frequencies [96–101]. In the typical growth conditions we consider here (metal on insulator at temperature above RT) the diffusion of adatoms is limited by desorption and the diffusion length $X_s$ of an adatom is:

$$X_s = (D\tau)^{1/2} = (a/2)\exp[(E_a - E_d)/2kT] \tag{15}$$

Then, one can consider that around each cluster exists a *collection zone* where every adsorbed will be captured by the growing cluster. In the case of an isolated cluster the width of the capture zone is close to $X_s$. Halpern has treated exactly the growth rate for an isolated cluster [96]. In order to take into account for the competition between growing clusters, Sigsbee and Stowell have used the lattice approximation [97, 98]. They consider that the growing clusters are sited on a regular square (or hexagonal) lattice, the growth conditions are the same for all clusters. In these conditions the density of adatoms around each cluster can be analytically solved [99]. Another way to treat this problem of the capture of adatoms: the uniform depletion approximation has been introduced by Lewis and Venables [99, 100]. In this treatment one considers a uniform density of clusters and the growth flux around each cluster is calculated assuming a uniform density of adatoms all over the substrate which is derived from the calculation of an isolated cluster by Halpern [96]. It has been shown that the uniform depletion approximation is a rather good approximation of the lattice model [101]. In a general case the growth rate of clusters can be calculated only numerically. However in some cases, the capture number ($\sigma$) can be expressed then an explicit growth law can be obtained, as shown by Kashchiev [102, 103]. In the case of an isolated cluster, *i.e.* $L/X_s \gg 1$, $L$ is the mean half distance between two neighbouring clusters (incomplete condensation regime) and if the direct impingement is negligible (*i.e.* early stage of growth) the cluster radius varies with $t^{1/3}$ for 3D clusters [103] and $t^{1/2}$ for 2D clusters [102]. At late stage of growth (*i.e.* very large clusters) the clusters grow practically only by direct impingement then the radius vary linearly with time [103].

Another limiting case corresponds to the situation of a strong competition between clusters for capture of adatoms (*i.e.* $L/X_s \gg 1$: complete condensation regime); the cluster radius varies with $t^{1/3}$ or $t^{1/2}$ for 3D and 2D clusters, respectively. In a general case the growth rate of a cluster can be expressed by a power law of the deposition time:

$$R(t) = R_o t^p \tag{16}$$

The exponent for any experimental has been calculated in the case of the lattice approximation for 3D clusters [104]. Figure 12 displays the exponent p as a function of the reduced radius ($R/X_s$) and for various value of the reduced cluster lattice parameter ($L/X_s$).

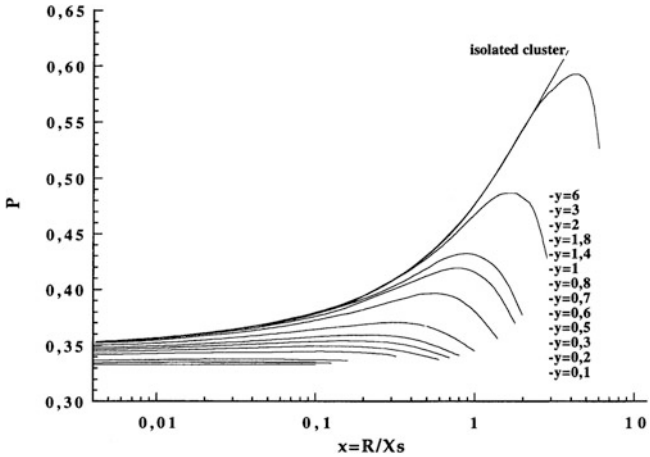


**Fig. 12** Exponent of the growth power law as a function of the reduced radius ($R/X_s$) and for various reduced intercluster half-distance ($y = L/X_s$). Top curve represent the case of an isolated cluster. From Ref. [104], copyright (1998), with permission from Elsevier

From this figure we immediately recognize the limiting cases: exponent close to 1/3 for incomplete condensation ($L/X_s$ small) and beginning of growth ($R/X_s$ small) and for complete condensation ($L/X_s$ large). However we can see on Fig. 12 that p is between 1/3 and 0.4 for a large range of values of $L/X_s$ and $R/X_s$, in agreement with experimental measurements for Pd clusters on various insulating substrates [104].

### 3.1.3 Nucleation and Growth on a Regular Lattice of Point Defects

The case of nanostructured substrate exhibiting a regular array of defects is a quasi-ideal system. Indeed, nucleation on defects is very rapid and then due to regularly spaced nuclei the growth rate will be uniform and as a consequence the size dispersion will be very narrow. In the recent years several naturally nanostructured substrates have been discovered like ultrathin films of alumina on $Ni_3Al(111)$ [105–107], ultrathin film of titania on Pt(111) [108] and CoO film on Ag(001) [109]. These nanostructured oxide substrates have shown to be good templates to grow arrays of metal clusters [107–112]. The nucleation and growth of metal clusters on a lattice of defects have been studied by kinetic Monte Carlo simulation (KMC) in the case of 2D and 3D growth [113, 114]. The energetic parameters used for the simulation of 3D growth correspond to the case of Pd clusters on nanostructured alumina on $Ni_3Al(111)$ [105–107]. Figure 13 displays the variation of the saturation density as a function of the substrate temperature. The simulation shows a rapid nucleation on the defects until a complete occupation but only in the temperature range 240–300 K. At higher temperature some

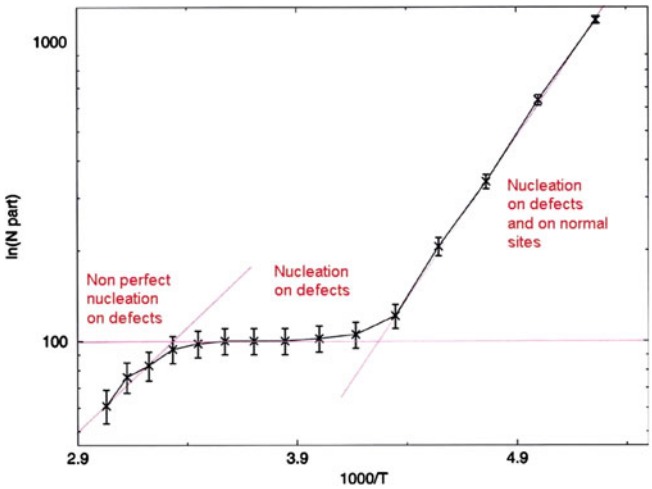


**Fig. 13** Variation of the saturation density of clusters versus reciprocal temperature calculated by KMC simulation for Pd/alumina/$Ni_3Al$(111). Adapted from Ref. [114], copyright (2010), with permission from Elsevier

defects remain empty because they are no longer perfect sinks for adatoms. At very low temperature nucleation occurs also on regular adsorption sites and the density of clusters is larger than the density of defects. After the nucleation stage clusters grow uniformly that results in a very sharp size distribution (size dispersion around 7% of the mean size) [114].

### 3.1.4 Nucleation and Growth of Bimetallic Clusters (AB)

**Case of simultaneous deposition**

The case of nucleation on a homogeneous substrate with a critical nucleus of one atom has been for the first time treated by Anton and Harsdorff [115]. One has to add the nucleation of AA, BB and AB dimers. However, now it is known that for insulator substrates we are interested here (metal oxides, alkali halides….) nucleation is controlled by defects.

Considering a nucleation on point defects the total nucleation rate is the sum of the nucleation of A and B which are given by Eqs. (12) and (13):

$$\begin{aligned} J &= J_A + J_B \\ &= (\sigma_A a^2 F_A/4)\exp[(E_{aA} - E_{dA})/kT] + (\sigma_B a^2 F_B/4)\exp[(E_{aB} - E_{dB})/kT] \end{aligned} \quad (17)$$

In a general case the energetic terms are different then nucleation of one species will dominate. The growth rate is calculated by summing the contribution of the two metals given by the growth kinetics of monometallic clusters (Sect. 3.1.2). Like in the case of a single metal, power laws are also expected [92, 116].

The time dependence of the chemical composition can be also obtained in integrating the growth equations but it can be also obtained more simply if the experimental growth law is known by adding the two contributions to the growth: direct impingement and capture of diffusion of adatoms. The first contribution is obvious and the second one can be calculated in the approximation of the *collection zone* [92].

**Case of sequential depositions (A, then B)**
Nucleation of A will take place. Still assuming nucleation on point defects, if at the end of the first deposition all defects sites are not occupied, during the second deposition there will be competition between nucleation of B and growth of bimetallic AB clusters. The relative rates of these two processes will depend on the relative values of the adsorption and diffusion energies which depend on the strength of the metal substrate interaction. If interaction of B with the substrate is weaker than those of A, growth will be favoured. It will also depend of the density of nuclei. A higher density will favour growth of bimetallic particles. The growth rate of bimetallic clusters, will be given by Eq. (16) with an initial condition which is the size of the pure A cluster at the end of the first deposition.

## *3.2 Nucleation and Growth of Bimetallic Clusters: Experiments*

### 3.2.1 Simultaneous Deposition

The $F_A$ and $F_B$ fluxes of atoms A and B impinge simultaneously on the substrate. For the nucleation stage the two types of atoms compete for the occupation of nucleation sites: this competition depends on the flux ratio $F_A/F_B$ and the relative values of the adsorption energy of the two types of atoms $E_{aA}$ and $E_{aB}$. If adsorption energy of A is significantly larger than the one of B, the nucleation is dominated by the A species. Assuming nucleation on defects, rapidly all the defects are filled by A-rich clusters then bimetallic clusters will grow by capture of A and B adatoms (dominant at the early stages of growth) or by direct impingement (dominant at late stage of growth). Thus the composition of the clusters will start from pure A up to the nominal composition which $Z_{A\infty} = F_A/(F_A + F_B)$. Table 1 displays examples of growth studies of bimetallic clusters on insulators by simultaneous depositions.

The first systematic studies on the nucleation have been performed by the group of Anton [116–121]. For these early studies, scanning probe microscopy techniques were not yet invented and (ex situ) TEM was the main technique of characterization of the bimetallic nanoparticles. By TEM the size distribution, the structure and the morphology of the nanoparticles can be determined [46]. The composition can be determined with a TEM by X-Ray fluorescence [116, 122] and on the modern (S)TEM by HAADF and EELS [123] techniques at the level of a single particle. Anton's group has investigated several types of bimetallic

**Table 1** Simultaneous deposition of the two metals (A,B). $\mathbf{\Delta H_{sublimation}}$ is the sublimation energy of the pure metal indicated in the order A/B. **Z = f(t)** means the chemical composition evolves during the deposition of the two metals, eventually after a long time the nominal composition can be reached. **A segreg.** means that A segregates at the particle surface

| AB | FePt | AuPd | CuPd | AgPd | AuCu | AuAg |
|---|---|---|---|---|---|---|
| $\Delta H_{sublimation}$ (eV/atom) | 5.85/4.29 | 3.94/3.78 | 3.94/3.50 | 3.94/2.91 | 3.78/3.50 | 3.78/291 |
| Substrate | NaCl(100) | NaCl(100) $CeO_2$/Ru(0001) $Fe_3O_4$/Pt(111) MgO/Ag(100) | NaCl(100) | NaCl(100) | NaCl(100) | NaCl(100) KBr(100) |
| Techniques | AFM TEM/EDX | TEM/EDX IRAS,TPD | TEM/EDX | TEM/EDX | TEM/EDX | TEM/EDX |
| Results, references | FePt alloy [126] | AuPd alloy Z = f(t) Au segreg. [119–121, 128] | CuPd alloy Z = f(t) [92, 124, 125] | AgPd alloy Z = f(t) [119, 120] | AuCu alloy Z = f(t) [118] | AuAg alloy Z = f(t) [116, 117] |

nanoparticles: AuPd [119–121], AgPd [119], AuCu [118], AuAg [116] on UHV-cleaved NaCl. The AuPd system has been studied in details. Figure 14 displays the evolution of the Au content in the nanoparticles as a function of the deposition time and for various ratios $F_{Pd}/F_{Au}$. It is clear that during the first stages of growth the nanoparticles contain mainly Pd [120]. This result is due to the much larger adsorption energy of Pd on NaCl compared to Au. By increasing the flux of gold atoms the initial concentration of Au in the particles increases but for all flux ratios the composition of the nanoparticles evolves with deposition time. The nominal composition $Z_{A\infty}$ is eventually reached for a ratio $F_{Au}/F_{Pd} = 16.3$ after about one hour of deposition that would correspond to very large particles ($D = 40$ nm [121]). The composition has been also determined from Monte Carlo simulation for the early stages of growth of the nanoparticles (the capture numbers are assumed to correspond to the isolated cluster limit, see Sect. 3.1.2) and a good agreement with experiment (Fig. 14) has been obtained with adsorption energies of 0.78 and 0.48 eV for Pd and Ag, respectively.

The growth of CuPd on UHV-cleaved NaCl has been also studied by TEM and EDX in the Henry's group [92, 124, 125]. Figure 15 displays the Cu concentration as a function of time for a flux ratio $F_{Cu}/F_{Pd} = 8$ [92]. Again, as the interaction of Pd with NaCl is much larger than those of Cu, nucleation is dominated by Pd and the particles become enriched in Cu during their growth. The nominal concentration (88.8% of Cu) is not reached after 900 s of deposition.

Figure 16 displays the nucleation kinetics and the growth rate of CuPd nanoparticles. The nucleation kinetics follows the nucleation on defects behaviour (see Eq. (13)): the density of clusters reached rapidly a saturation value. The nucleation kinetics is very close to the case of pure Pd [92], showing that for Pd and Cu simultaneous deposition the nucleation is controlled by Pd. The growth

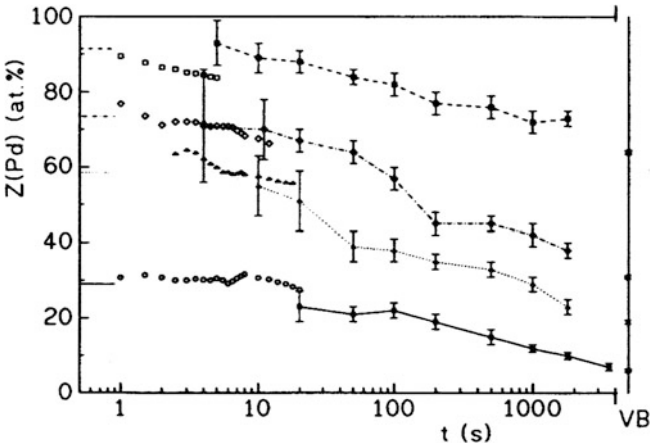


**Fig. 14** Semi-logarithmic plot of the concentration of Pd in AuPd nanoparticles grown on NaCl(001) by simultaneous deposition of Au ($F_{Au} = 4.4 \times 10^{13}$ cm$^{-2}$ s$^{-1}$) and Pd (from the top to the bottom curves $F_{Pd} = 7.9$, 2, 1 and $0.27 \times 10^{13}$ cm$^{-2}$ s$^{-1}$) as a function of deposition time. The solid symbols correspond to experimental measurement by EDX and the open symbols correspond to MC simulation. From Ref. [120], copyright (1990) by The American Physical Society

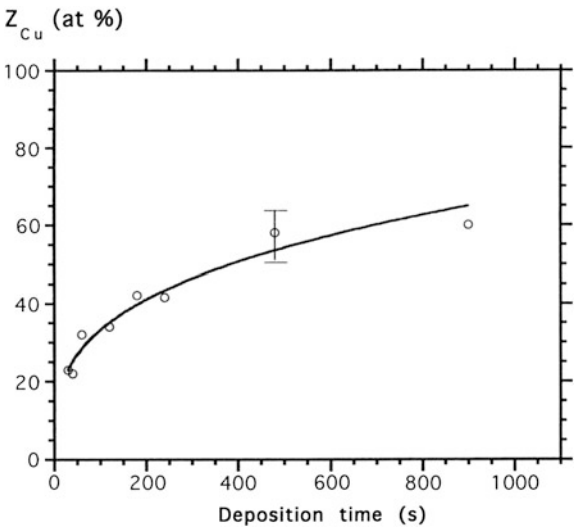


**Fig. 15** Variation of the concentration of Cu in CuPd clusters grown on NaCl(001) by simultaneous deposition of Pd ($F_{Pd} = 1 \times 10^{13}$ cm$^{-2}$ s$^{-1}$) and Cu ($F_{Cu} = 8 \times 10^{13}$ cm$^{-2}$ s$^{-1}$) at 553 K as a function of deposition time, measured by EDX. From Ref. [92], reproduced by permission of the Royal Society of Chemistry

rate of CuPd clusters follows a power law with an exponent of 0.42 close to the case of pure Pd (0.40). These results prove two facts: (i) the growth mainly occurs by capture of atoms adsorbed on the NaCl substrate which is expected because the substrate coverage is low (smaller than 5%), (ii) the capture of Cu adatoms is weak.

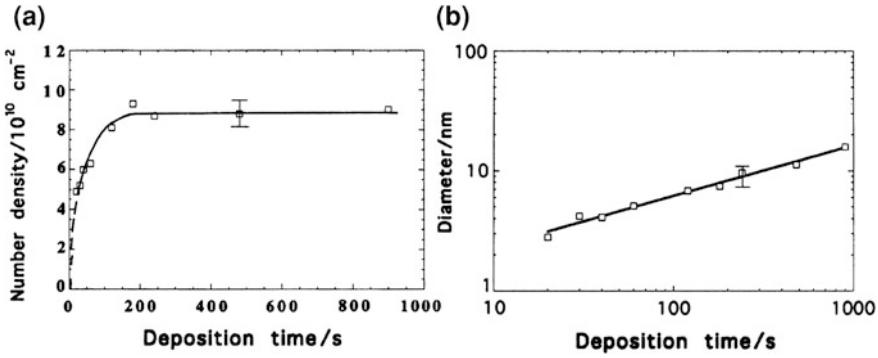


**Fig. 16** Nucleation (**a**) and growth kinetics (**b**) of CuPd clusters on NaCl(001) by simultaneous deposition of Pd ($F_{Pd} = 1$ x $10^{13}$ cm$^{-2}$ s$^{-1}$) and Cu ($F_{Cu} = 8$ x $10^{13}$ cm$^{-2}$ s$^{-1}$) at 553 K as a function of deposition time. From Ref. [92], reproduced by permission of the Royal Society of Chemistry

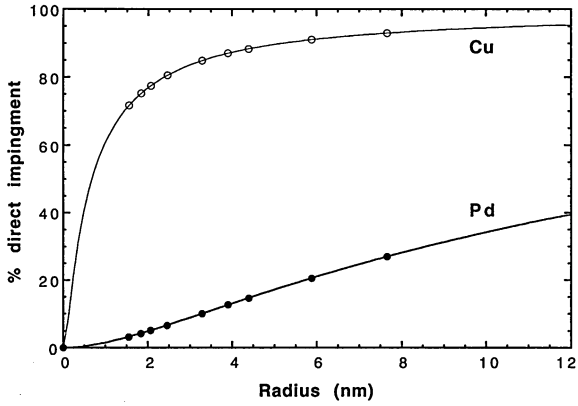


**Fig. 17** Percentage of direct impingement for Cu and Pd during the growth of CuPd clusters on NaCl(001) by simultaneous deposition of Pd ($F_{Pd} = 1 \times 10^{13}$ cm$^{-2}$ s$^{-1}$) and Cu ($F_{Cu} = 8 \times 10^{13}$ cm$^{-2}$ s$^{-1}$) at 553 K as a function of deposition time. From Ref. [92], reproduced by permission of the Royal Society of Chemistry

In order to determine the energetic parameters ($E_a$ and $E_d$) for this system the growth of the bimetallic particles has been simulated by using the lattice approximation (see Sect. 3.1.2). From the fit of the growth kinetics and of the time dependent composition with this growth model the ($E_a - E_d$) parameters of 0.38 and 0.07 eV have been determined for Pd and Cu, respectively [92]. Once these parameters have been determined it becomes possible to know the relative contribution of the two growth mechanisms (direct impingement and capture of adatoms) during the growth for the two types of atoms. Figure 17 shows the proportion of incorporation of Pd and Cu atoms by direct impingement during the growth of the CuPd clusters. We see clearly that Cu is mainly incorporated by direct impingement while Pd is mainly incorporated by capture of adatoms. This becomes clear if we consider that at the growth temperature (553 K) the mean diffusion length of Cu is very small (0.5 nm) while it is much larger for

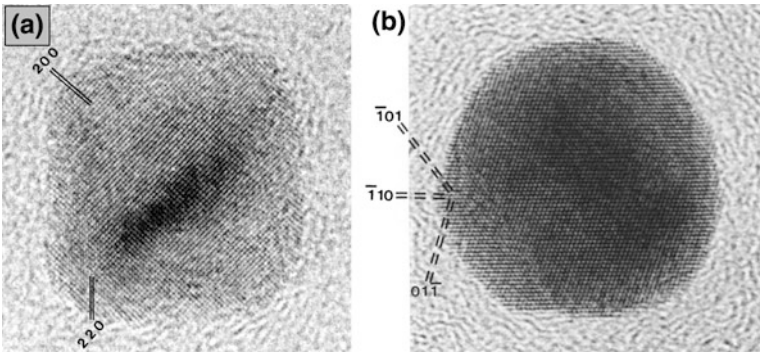


**Fig. 18** HRTEM pictures of CuPd nanoparticles grown by simultaneous deposition on NaCl. **a** After growth at 553 K. **b** After annealing at 638 K. From Refs. [124, 125]

Pd (7.5 nm) in comparison with the size of the clusters (the relative contribution of the diffusion-capture process to the direct impingement is roughly equal to $2X_s/R$).

The structure of the nanoparticles can be determined by HRTEM. In the case of CuPd/NaCl(001) the particles grown at 553 K have a face centered cubic structure that corresponds to a solid solution *i.e.* no chemical order (see Fig. 18a). After annealing at 638 K the particles get the CsCl type structure corresponding to the ordered CuPd structure (see Fig. 18b) [125].

The growth of bimetallic nanoparticles by simultaneous deposition of the two metals has rarely been studied by AFM or STM [126–128]. In the case of FePt/NaCl [126] the nanoparticles were characterized by a combination of in situ STM, ex situ TEM, TED and EDX which show that the particles were bimetallic and epitaxied on the NaCl substrate, the average composition was determined.

In summary, for simultaneous deposition, the composition of the bimetallic particles evolves during the growth except at the late stage of growth when the direct impingement is the main growth mechanism where the concentration tends to the nominal one. The variation of the composition is due to the different incorporation of the two metals which is related to the width of the capture zone around the clusters which depends exponentially on the energetic parameter $E_a - E_d$ which varies with metal substrate interaction. In principle it could be possible to correct for this difference of capture rate by increasing the flux of the metal having the weaker interaction but in practice it is necessary to adjust continually the flux ratio that would be very difficult to manage.

### 3.2.2 Sequential Deposition

In the case of sequential deposition, A then B, the nucleation is controlled by A but during the second deposition metal B can nucleate new pure B clusters or only grow pre-existing A clusters. The competition between these two processes

depends on the metal-substrate interactions but also on the distance between prenucleated clusters. If the prenucleated A clusters occupy all the defects sites which are separated by a distance much smaller than the diffusion length ($X_s$) of an adsorbed B atom the growth of AB clusters will dominate. If the mean diffusion length of B atoms is smaller than the distance between A clusters the growth of A clusters will be negligible. Finally if some defects are not occupied by A clusters nucleation of B clusters will occur. We will see all these possibilities by looking on the published works in the recent years (Table 2) which use mainly STM as a charaterization tool of the nanoparticles.

CoPd is the most studied systems [129–132]. The CoPd particles are grown on an ultrathin alumina thin film obtained by high temperature oxidation of NiAl(110) by depositing sequentially Co then Pd or Pd then Co. The particle nucleation and growth were investigated in situ by STM. By depositing first Co then Pd, the density of clusters stays unchanged after the second deposition and the mean size of the clusters increases, that means that no nucleation of pure Pd occurred and that Pd participates only in the growth of bimetallic clusters [129, 132]. In the reverse case, Pd deposition then Co deposition, after the second deposition the density of clusters increases by about 30% and the size of clusters increases [129, 132]. In this case new pure Co clusters are formed together with bimetallic CoPd clusters. For Fe deposited on Pd preformed clusters, pure Fe clusters are observed together with bimetallic ones, in the reverse order only bimetallic clusters are observed [133]. If now Au [111, 134] or Ag [135] is deposited on prenucleated Pd clusters one get only bimetallic particles (no new clusters are formed) on the contrary if Pd is deposited on Au prenucleated clusters one obtains pure Pd and bimetallic AuPd particles [136]. These different behaviours can be rationalized if one compare the sublimation energy of the different metals (see Table 2) which roughly scales with the interaction of the metal with the substrate. The sublimation energy of Pd is smaller than those of Co or Fe and larger than those of Ag or Au. During the first deposition the nucleation rate (*i.e.* the number of formed clusters) for Co or Fe will be much larger than for Pd and the nucleation of Pd will be larger than for Ag or Au. Assuming a predeposition of Pd clusters, in the second step the competition between nucleation of Co or Fe and growth of bimetallic clusters will be in favour of the nucleation of pure Co or Fe clusters. In the case of Au or Ag the nucleation of pure Au or Ag will be disfavoured by a low nucleation rate and fast diffusion of adatoms that will prefer to grow prenucleated Pd clusters.

However, in the case of nucleation on point defects and assuming that they act as perfect sinks for adatoms, nucleation of Au or Ag can occur except if all the defects were already occupied by Pd and then no nucleation could occur [111]. The same reasoning holds in the case of deposition of Pd on prenucleated Co or Fe clusters.

On Fig. 20 we see the effect of the cluster density after the first deposition (Ag) for the system Au/Ag on $TiO_2$(110) which has been studied in situ by STM [137]. Figure 19 displays a series of STM images from the same area after deposition of Au on prenucleated Ag clusters. The observation of the same area is a clear advantage because it becomes possible to see the individual mechanisms:

**Table 2** Sequential deposition of the two metals (A,B). $\Delta H_{sublimation}$ is the sublimation energy of the pure metal indicated in the order A/B. For the deposition order **A/B** means that A metal is deposited on pre-nucleated B clusters, for the results AB means bimetallic particle, **A or B** means pure A or B particles. **A segreg.** means that A segregates at the particle surface

| AB | PtRh | CoPd | FePd | AuPd | AgPd | AuAg |
|---|---|---|---|---|---|---|
| $\Delta H_{sublimation}$ (eV/atom) | 5.85/5.75 | 4.39/3.94 | 4.29/3.94 | 3.94/3.78 | 3.94/2.51 | 3.78/2.91 |
| Substrate | $TiO_2$(110) | Alumina/ NiAl(110) | Alumina/ NiAl(110) | Alumina/ $Ni_3Al$(111), $TiO_2$(110) | Alumina/ NiAl(110) | $TiO_2$(110), Alumina/ NiAl(110) |
| Techniques | STM, LEIS | STM, AES LEIS, IRAS TPD | STM, XPS IRAS,TPD | STM | STM, XPS IRAS, TPD | STM, photon emission |
| Deposition order, results, references | **Pt/Rh** PtRh+Pt, [139] | **Co/Pd** CoPd (alloy/core–shell) + Co **Pd/Co** PdCo(core–shell) [129–132] | **Fe/Pd** FePd+Pd **Pd/Fe** PdFe(core–shell) [133] | **Pd/Au** AuPd+Pd [136] **Au/Pd** AuPd (Au segreg.) [111, 134] | **Ag/Pd** AgPd (Ag segreg.) [135] | **Au/Ag** AuAg(core-shell) + Au [137] **Ag/Au** AuAg [154] |

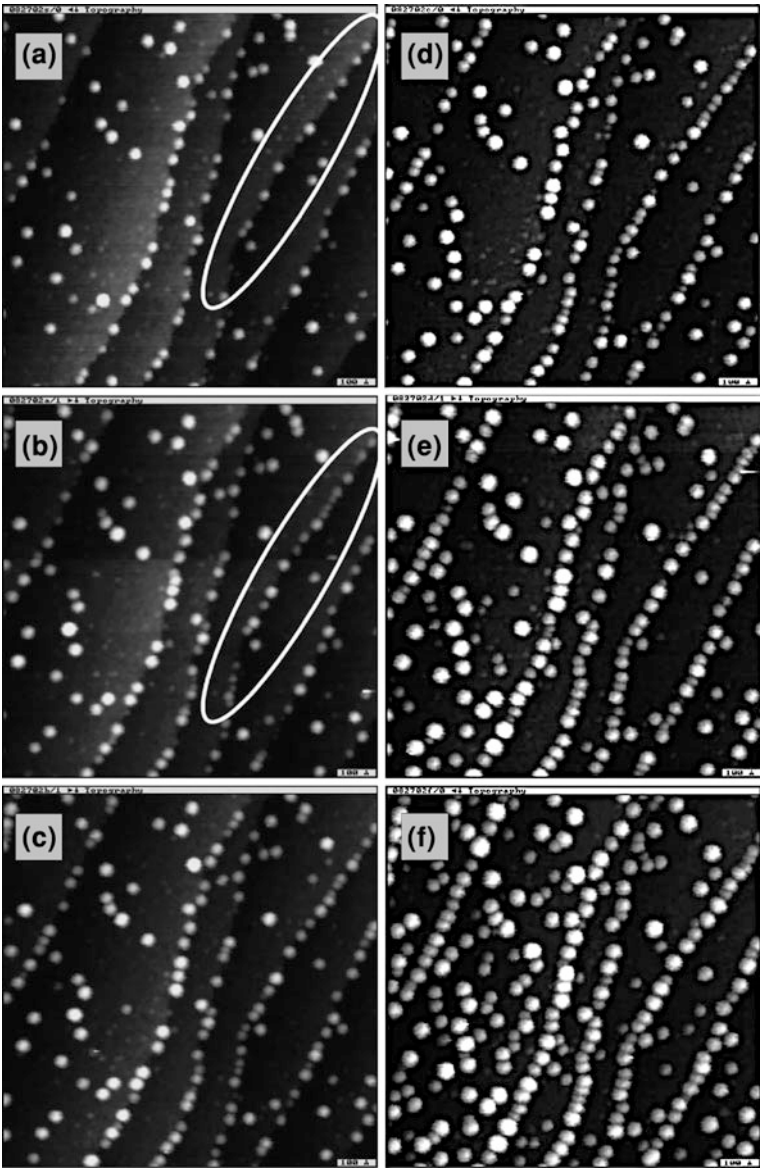


**Fig. 19** STM images of a series of depositions of Au (**b** 0.17, **c** 0.34, **d** 0.51, **e** 0.85 and **f** 1.53 ML) on prenucleated Ag clusters (**a** 0.033 ML) on $TiO_2$(110). From Ref. [137], copyright (2004), with permission from Elsevier

nucleation of a new cluster, cluster growth, cluster mobility, coalescence of two clusters. In this particular case it is also possible to distinguish between steps and terraces. By increasing the amount of deposited Au atoms it is clear that Ag

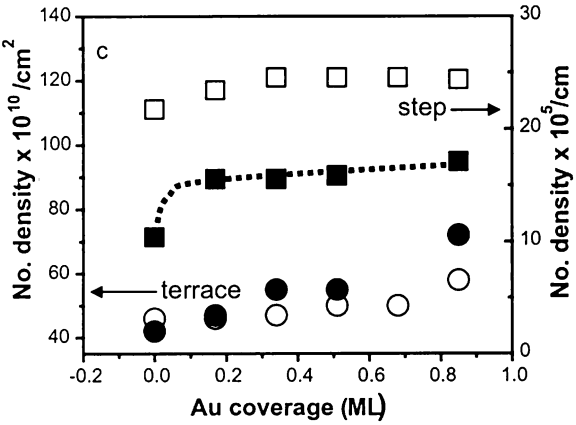


**Fig. 20** Variation of the cluster density on steps (*square*) and terraces (*circle*) as a function of the amount of deposited Au on Ag clusters prenucleated on $TiO_2(110)$ from two different coverages: 0.08 (*open symbol*) and 0.033 ML (*solid symbol*). From Ref. [137], copyright (2004), with permission from Elsevier

clusters grow and that new pure Au clusters appear. This is not surprising because the adsorption energy is larger for Au than for Ag (if we still scale with the sublimation energy—see Table 1).

From this study the density of clusters has been measured as a function of the amount of deposited gold both on terraces and on steps. We see on Fig. 20 that the density of clusters is larger on steps than on terraces that is a well known effect which is responsible for the step decoration phenomenon already observed in the first studies of metal deposition on ionic crystals [138]. On steps, by increasing the Ag coverage the density of clusters strongly increases showing that after the thinner Ag deposit the saturation density was far to be reached. Then, during Au deposition the density of clusters notably increased. For the thick Ag deposit the density of clusters is close to saturation and the density of clusters is more or less constant after Au deposition. On terraces, after the deposition of Ag at the lowest coverage (0.033 ML) the saturation density of clusters is more or less reached then the density of clusters increases only slightly during Au deposition. The density of defects is certainly much larger on steps than on terraces.

In the case where the interaction energies of the two metals with the support are very close the use of STM is very important to see which mechanisms occurs during the second deposition. Taking the case of Pt deposited on preformed Rh clusters on $TiO_2(110)$ [139], the sublimation energies of Pt and Rh are 5.85 and 5.75 eV/atom, respectively. Figure 21 shows a series of STM pictures after increasing the amount of Pt deposited on prenucleated Rh clusters. The density of clusters is very large after the deposition of Rh, after Pt deposition the main phenomenon is an increase of the cluster size. However a close examination of the successive pictures from the same area shows that some nucleation of pure Pt occurs but also in the same time some bimetallic clusters disappear by coalescence. Increasing deposition temperature, favours cluster growth relatively to nucleation of pure Pt as expected from nucleation theory (see Sect. 1).

The competition between growth of AB clusters and pure B nucleation depends also on the distance between prenucleated A clusters. Indeed if two clusters are

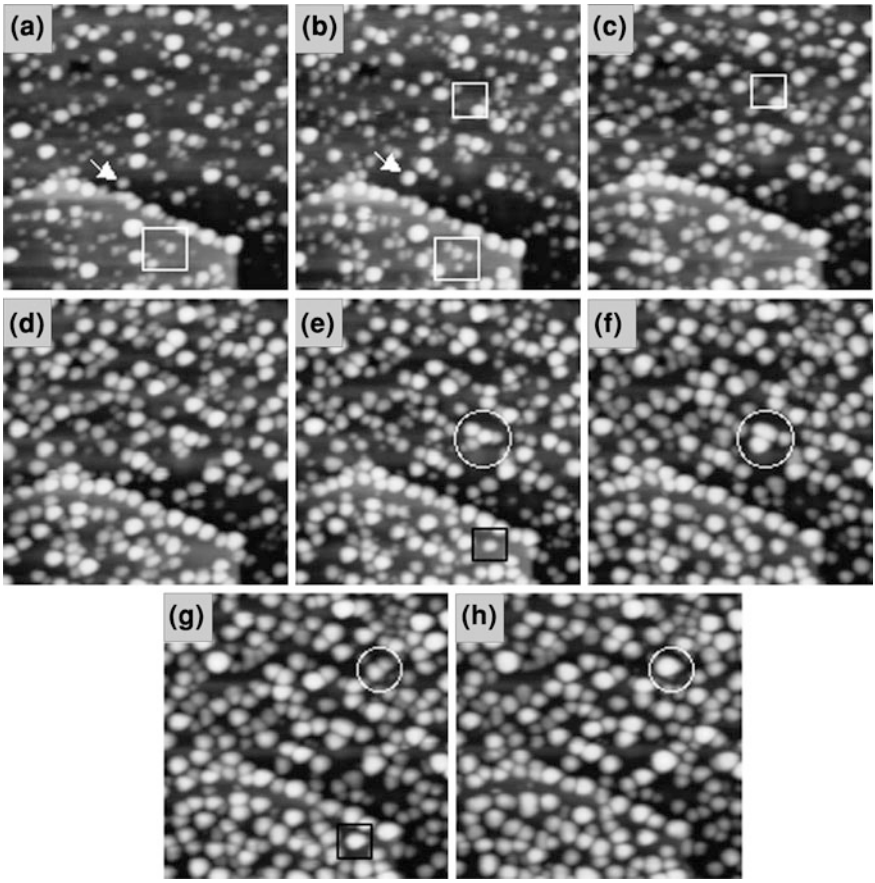


**Fig. 21** STM images (50 nm × 50 nm) on the same area of increasing amount of Pt deposited (**b** 0.09, **c** 0.18, **d** 0.33, **e** 0.51, **f** 0.88, **g** 1.18 and **h** 1.6 ML) on prenucleated Rh clusters (**a** 0.3 ML) on $TiO_2$(110). From Ref. [139], copyright (2006), with permission from Elsevier

very close nucleation of a new cluster has less chance to occur than in the case where the clusters are far each other. Conversely, if two clusters are very close they strongly compete for capture of adatoms. Therefore the composition of the clusters will not be homogenous on the substrate in the typical situation of randomly distributed defects. A way to avoid these problems is to have a substrate presenting a regular array of point defects. This situation occurs in the case of nanostructured oxide ultrathin films [105–109]. In this case the nucleation will occur rapidly on all the defects and when saturation is reached, the clusters will grow homogeneously on the whole substrate. Such a case is presented on Fig. 22. By depositing Au on prenucleated Pd clusters (at 0.1 ML the saturation density is reached at RT), in situ STM observation shows that the density of clusters is constant and the size dispersion is weak [111, 140] (see Figs. 22 and 23). However

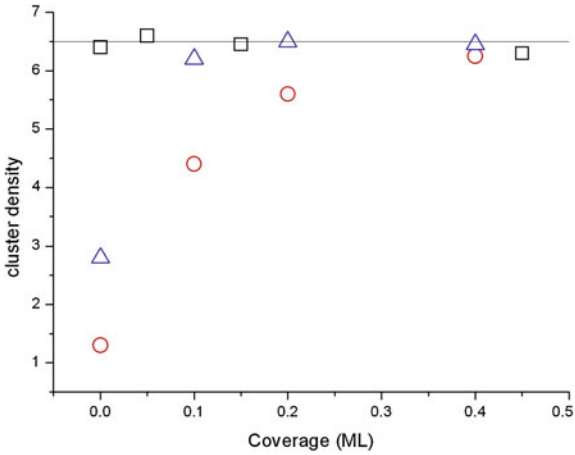


**Fig. 22** Au/Pd on alumina on $Ni_3Al(111)$: density of clusters as a function of coverage. *Square* Au on pre-nucleated Pd, *circle* Pd on 0.1 ML pre-nucleated Au, triangle: Pd on 0.2 ML pre-nucleated Au. The straight line corresponds to the saturation of the defects ($6.5 \times 10^{12}$ $cm^{-2}$). From Refs. [136, 140], reproduced by permission of the Royal Society of Chemistry

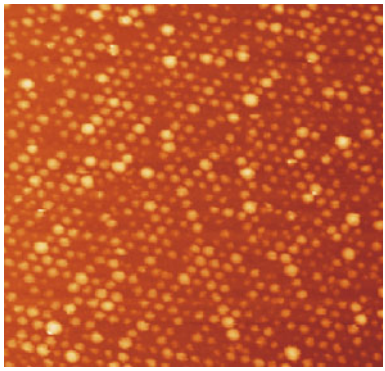

**Fig. 23** STM image (200 nm × 200 nm) of AuPd clusters obtained by deposition of 0.04 ML of Au on pre-nucleated Pd clusters (0.02 ML) on alumina on $Ni_3Al(111)$. From Ref. [111]

in the reverse case when Pd is deposited on prenucleated Au clusters, we see on Fig. 22 that the saturation density is not reached because the point defects are not perfect sinks for Au adatoms at RT and the density of clusters increases by formation of pure Pd clusters until all defects are occupied [136]. However by increasing the amount of predeposited gold the proportion of pure Pd clusters decreases. Taking into account the fact that the point defects are not perfect sinks for Au adatoms, during the gold deposition on prenucleated Pd clusters below the saturation density, growth of bimetallic clusters will mainly occur because gold atoms can escape from the defects while they stick permanently to preformed Pd clusters [111].

## Cluster Shape

STM and AFM are well suited techniques to study in situ the nucleation and growth of bimetallic clusters while TEM techniques are limited to ex situ observation. However scanning probe techniques (AFM, STM) are a severe limitation which is due to the deformation of the object by the shape of the scanning tip that

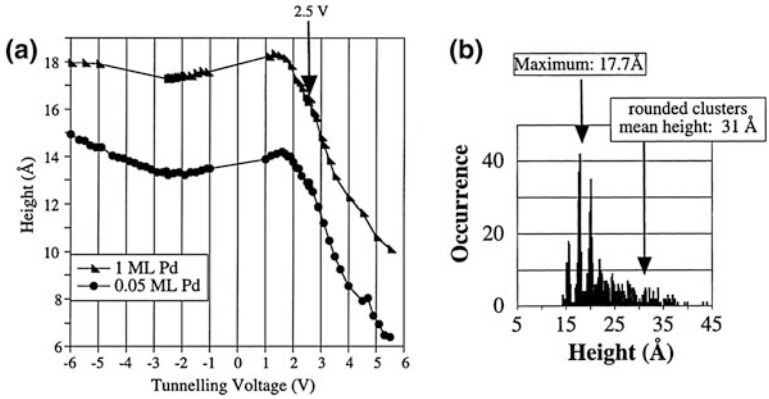


**Fig. 24** STM imaging of Pd clusters grown on a ultrathin alumina film on NiAl(110). **a** Apparent height as a function of bias voltage for coverage of Pd of 1 and 0.5 ML. **b** Height distribution. The different peaks separated by roughly 0.22 nm correspond to integer numbers of layers. From Ref. [132], copyright (2007), with permission from Elsevier

leads to an increase of the apparent size and rounding of the shape. This effect and some alternatives are discussed in the first part of the paper (see Sect. 2.3). Often it is believed that height measurements are very accurate by STM. This is true for metallic samples after calibration of the microscope. However in the case of metal clusters supported on an insulting ultrathin film the situation is not so clear. Figure 24a displays the measured height as a function of bias voltage for two deposits of Pd on alumina on NiAl(110) [132]. At negative or low positive value of the bias voltage the cluster height is nearly constant but at voltage larger than 2 V the height strongly decreases. In fact at positive voltage higher than 2.2 V the tip probe unoccupied states of the oxide film then the measured height is no longer representative of the true height of the Pd clusters. However below the band gap of the oxide the tunnelling current comes only from Pd states from the clusters. In order to calibrate accurately the height scale, one can measure the height histogram from a large number of clusters (see Fig. 24b). After these calibration a systematic correction of 0.3 nm is applied for height measurements at a bias voltage of 2.5 V [132]. A similar dependence of the apparent cluster height as a function of the bias voltage has been observed for Pd clusters on alumina on $Ni_3Al(111)$ [141].

Figure 25 displays an STM image of PdCo clusters on an ultrathin alumina film on NiAl(110) which are obtained by depositing 1 ML of Co on prenucleated Pd clusters (1.25 ML). Two types of clusters are visible: large facetted ones corresponding to bimetallic clusters and small round ones that correspond to pure Co clusters [132]. The large bimetallic clusters have a top truncated tetrahedron shape. The top facet is flat and atomic resolution have been obtained (see Fig. 25b) it corresponds to a (111) plane [132]. The atomically resolved image presents bright atoms and dark ones. They are identified from previous studies of Co atoms

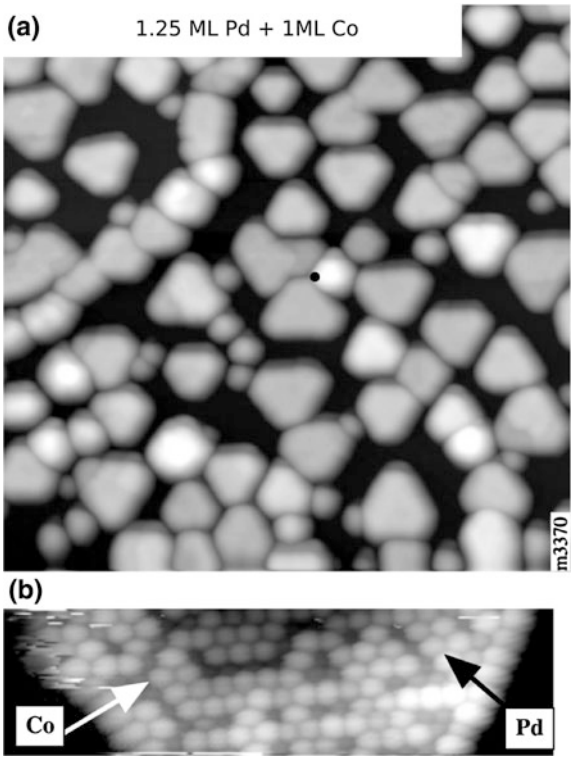


**Fig. 25** STM images of 1 ML of Co deposited on prenucleated Pd clusters (1.25 ML) on a ultrathin alumina film on NiAl(110). (**a**) 100 nm × 100 nm area (**b**) atomically resolved image of a top (111) facet of a PdCo cluster showing chemical sensitivity. From Ref [132], copyright (2007), with permission from Elsevier

deposited on Pd(111) to Pd and Co atoms, respectively [132]. This image shows that by depositing Co on Pd clusters at RT alloy is formed instead of core shell structure. Thus segregation of Pd toward cluster surface is possible at RT while in the bulk segregation occurs above 300°C [142]. Atomic resolution with chemical sensitivity on top facets of bimetallic particles is the ideal method to study surface composition at the level of one particle. However, it is very difficult task and from the best of our knowledge it has been reported only once for PdCo nanoparticles [132]. Other techniques like LEIS, MEIS can provide such information on a collection of bimetallic particles. LEIS is the acronym for low energy ion scattering uses ion energies between 1 and 5 keV and probes only the top surface of the nanoparticles (see Ref. [143] for details on the technique). By LEIS it has been shown in the case of AuPd bimetallic particles that Au has a tendency to segregate at the surface of the particle [144] as expected from surface energy consideration and observed on single crystal alloys. MEIS (medium energy ion scattering) uses more energetic ions (50–200 keV) and thus provides information about the surface and the bulk composition of the nanoparticles [145]. It has been confirmed by MEIS that in AuPd nanoparticles Au segregates on the surface (in agreement with AuPd particles prepared by simultaneous deposition [128]) and that subsurface layer is enriched in Pd [146]. Surface composition can also be indirectly studied by IRAS (infrared

reflection absorption spectroscopy) and TPD (thermal programmed desorption). In this case CO is (in situ) adsorbed on the nanoparticles and the stretching frequency or the binding energy of CO adsorbed on the A and B metal atoms are probed by IRAS or TPD, respectively. If the stretching frequencies or the binding energies are different for the two types of atoms in principle, the surface composition can be obtained. However the interpretation of the spectra is not so straightforward. Firstly, CO adsorption can induce surface segregation (the metal which has the largest binding with CO tends to be at the surface). CO adsorption induced segregation has been observed for CuPd [147] and AuPd nanoparticles [148]. Secondly, the CO stretching frequency is influenced by CO coverage and environment of a given atom which changes with surface composition. For these reasons these two techniques provide mainly qualitative information like for example presence of a core shell structure or an alloy. Combination of IRAS and TPD has been used to study sequentially grown PdCo [130, 131], PdFe [133] and AgPd [135] nanoparticles. For the three systems if the metal with the lower surface energy [149] is deposited in the second step it stays at the surface. If the metal with the higher surface energy is deposited in the second step, the first deposited metal segregates on the surface as for Fe/Pd while it is not exactly the case for Co/Pd where part of Co stays at the particle surface although some Pd segregates on the surface and eventually Co cover the PdCo particles at very high Co coverage (2 nm Co/0.1 nm Pd) [131]. In Co/Pd, it was observed by chemically resolved STM images and by LEIS that Pd tends to segregate on the surface of bimetallic particles [132].

Much less studies on the growth of bimetallic nanoparticles have been performed by AFM than by STM. This is partly due to the fact that STM is an older technique than AFM but also by the fact that for in situ surface studies AFM is generally restricted to bulk insulator for which STM is inapplicable because STM is easier to operate and atomic resolution is much more difficult to reach by AFM than by STM. However in the recent years non contact AFM has made major advances [41] and in some cases nc-AFM has a better resolution than STM, for instance in imaging atoms of an adsorbed molecules [150]. Moreover, chemical identification of atoms can be performed at RT with systematic investigation of $\Delta f$ versus distance curves [43] (see Sect. 2.2 and Fig. 4a). Concerning the bimetallic nanoparticles on insulators few studies using AFM have been published in the recent years. The first one concerned the growth of FePt nanoparticles on NaCl surfaces [126]. Figure 26a displays an AFM picture of the bimetallic nanoparticles obtained by simultaneous deposition of the two metals. The particles appear more or less round and some are square, their apparent mean size is around 8 nm and their mean height is 5.5 nm (Fig. 26b). By TEM the particle size is between 6 to 7 nm and their outline is square or rectangle (Fig. 26c). The shape observed by AFM is less precise than by TEM because of the effect of the convolution with the tip shape, as we have seen previously, but AFM brings an accurate measure of the particle height that is not possible with TEM except in transverse view or by tomography [151].

The second study reports on ex situ AFM observations of AuPd nanoparticles grown on silica/Si(100) through an ice buffer layer [127]. Another study concerns

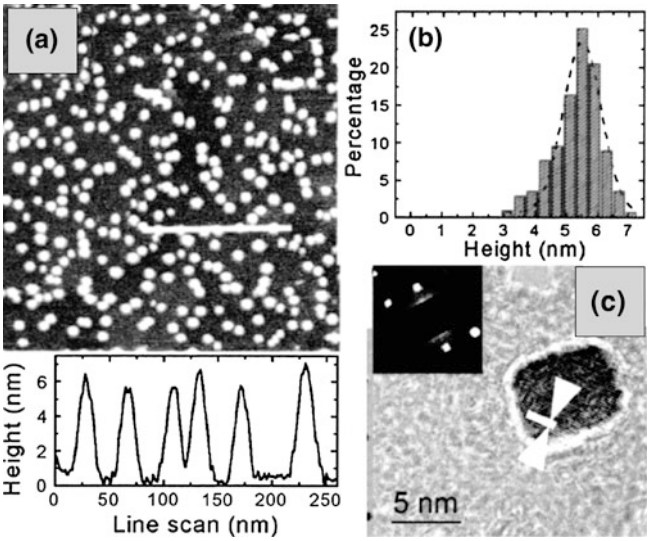


**Fig. 26** FePt bimetallic particles on NaCl(001) **a** AFM picture with a line profile at the *bottom* **b** height histogram **c** TEM picture of a single particle. From Ref. [126], copyright (2005), American Institute of Physics

bimetallic AuIn particles on a semiconductor surface [152]. Au is deposited at RT on InSb(001) and square Au islands are formed as observed in situ by nc-AFM. After annealing at 600 K the gold nanoparticles coalesce and larger square particles are obtained (see Fig. 27, top). In the KPFM mode (see Sect. 2.4) the particles show a contact potential difference of 10–20 mV (Fig. 27b, top). After annealing to 650 K the particle shape is the same but the difference of contact potential increases to 50–100 mV (see Fig. 27b, bottom). This large change in the contact potential difference is due to the formation of AuIn alloy nanoparticles. This interesting observation opens the way for a measurement of the composition of individual bimetallic nanoparticles. Indeed the contact potential difference measures (in the absence of permanent charges) the difference of work function between the substrate and the bimetallic particle (see Sect. 2.4). The work function of a bimetallic particle is expected to vary with its composition.

In summary some general rules can be drawn in the case of sequential deposition. In the case of deposition of B on pre-deposited A clusters:

- choose $E_{ad}(\mathrm{A}) > E_{ad}$ (B)
- A coverage sufficiently large to saturate all defects
- large $F_A$ to have fast nucleation
- choose a low deposition temperature of A to have fast nucleation but not too low to avoid homogenous nucleation
- choose a high deposition temperature of B to favour growth of prenucleated clusters.

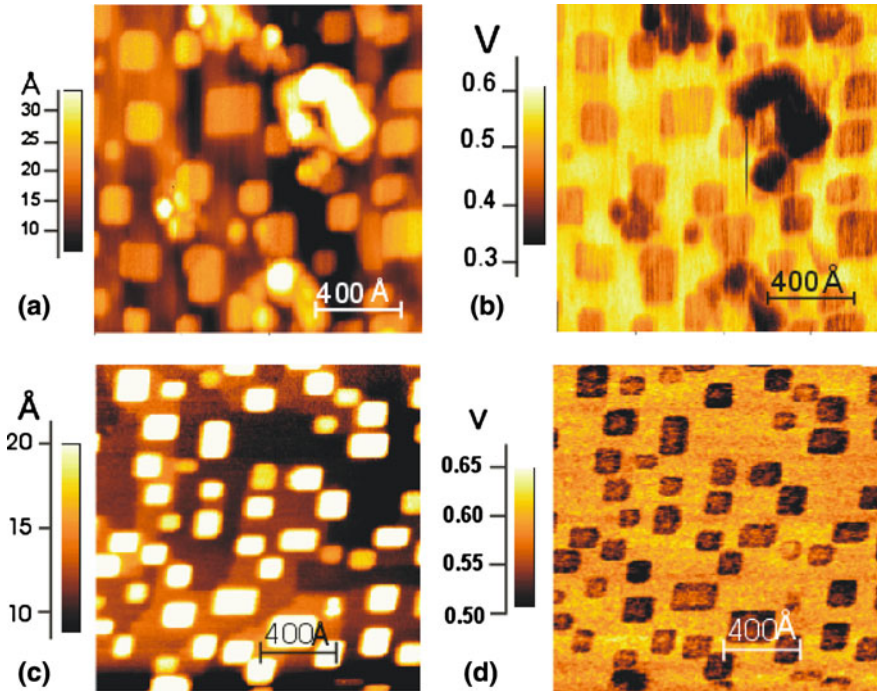


**Fig. 27** Non contact AFM images of Au particles grown at RT on InSb(001): top after annealing at 600 K, bottom after annealing at 650 K; topography (**a**) and Kelvin images (**b**). From Ref. [152], copyright (2004), with permission from Elsevier

The growth rate can be calculated by knowing $(E_a - E_d)_B$, the radius of the prenucleated clusters $R_A$ and their density $n_A$ by using the growth model (see Sect. 3.1.2 and Ref. [104]).

## Conclusion and Perspectives

STM and AFM are best suited techniques to study in situ the nucleation and growth of supported bimetallic clusters (STM is limited to bulk conducting substrates and ultrathin insulating films supported on metals whereas AFM can be used on any substrate surface). The morphology of the bimetallic nanoparticles can be studied by these two techniques but with some limitations. The size of the particles is enlarged and the shape is rounded on the edges by the interaction with the tip (tip-object convolution). This effect is often increased in AFM because the commercial tips are generally bigger than the STM ones. In non-contact AFM the actual shape can be revealed (at least the top facet) by using the constant height mode. The shape characterization by scanning probe microscopies can be completed by using integral techniques like GISAXS (grazing incidence small angle X-ray scattering) which can also be operated in situ during growth [153] or ex situ by TEM. The substrate surface can be easily imaged with atomic resolution

by AFM and STM but it is more difficult on the nanoparticles except for large facetted particles. The resolution of the facet structure could certainly be improved by working with functionalized tips. The determination by STM and AFM of the surface chemical composition of the bimetallic particles is still a big issue, but recent works on surface alloys have shown that atomic resolution with chemical sensitivity can be achieved with both techniques. Again a better understanding and control of the scanning tip is necessary to achieve routinely chemical sensitivity at atomic scale. Otherwise KPFM could become a technique to analyse surface composition on large facets. Nevertheless complementary integral surface science techniques are still necessary to fully characterize supported alloy nanoparticles, like LEIS (surface composition), MEIS (surface and bulk composition). Other techniques can provide some information on the surface composition of the nanoparticles after adsorption of molecules (typically CO) like IRAS or TPD but care has to be taken in order to avoid artefacts like surface segregation induced by the adsorbate. At the level of a single particle ex situ TEM techniques (EDX, EELS, HAADF) can provide quantitative information on the bulk composition of the particles.

From theory side, atomistic nucleation theory is well adapted to treat accurately the nucleation and growth of bimetallic clusters by deposition of atoms on an insulator substrate. It can provide analytic kinetic laws for nucleation and growth and the evolution of the chemical composition can be predicted. From the two modes of deposition: simultaneous and sequential the latter one is preferred because the composition can be more easily controlled. However for sequential composition it is important to choose correctly the order of deposition of the two metals and the deposition parameters (flux, substrate temperature). Again atomistic nucleation and growth theory can guide these choices. Two crucial parameters of this theory are the adsorption energy and the diffusion energy of adatoms. They are related to the interaction of the metal with the substrate. For a same substrate, the trends for different metals can be given by the cohesion energy of the metal. Besides nucleation-growth theory atomistic simulations can provide precious information about chemical order and segregation in bimetallic nanoparticles that can be different that for their bulk counterpart (see Chap. 8).

## References

1. Binnig, G., Rohrer, H., Gerber, Ch., Weibel, E.: Surface studies by scanning tunneling microscopy. Phys. Rev. Lett. **49**, 57 (1982)
2. Hansma, P.K., Tersoff, J.: Scanning tunneling microscopy. J. Appl. Phys. **61**, R1 (1986)
3. Feenstra, R.M.: Scanning tunneling spectroscopy. Surf. Sci. **299–300**, 965 (1994)
4. Komeda, T.: Chemical identification and manipulation of molecules by vibrational excitation via inelastic tunneling process with scanning tunneling microscopy. Prog. Surf. Sci. **78**, 41 (2005)
5. Tsukada, M., Kobayashi, K., Isshiki, N., Kageshima, H.: First-principles theory of scanning tunneling microscopy. Surf. Sci. Rep. **13**, 265 (1991)

6. Hofer, W.A., Foster, A.S., Shluger, A.L.: Theories of scanning probe microscopes at the atomic scale. Rev. Mod. Phys. **75**, 1287 (2003)
7. Wiesendanger, R.: Scanning Probe Microscopy and Spectroscopy. Cambridge University Press, Cambridge (1994)
8. Chen, C.J.: Introduction to Scanning Tunneling microscopy. Oxford University Press, New York (2008)
9. Africh, C., Kohler, L., Esch, F., Corso, M., Dri, C., Bucko, T., Kresse, G., Comelli, G.: Effects of lattice expansion on the reactivity of a one-dimensional oxide. J. Amer. Chem. Soc. **131**, 3253 (2009)
10. Crommie, M.F., Lutz, C.P., Eigler, D.M.: Confinement of electrons to quantum corrals on a metal surface. Science **262**, 218 (1993)
11. Varga, P., Schmid, M.: Chemical discrimination on atomic level by STM. Appl. Surf. Sci. **141**, 287 (1999)
12. Hallmark, V.M., Chiang, S., Rabolt, J.B., Swalen, J.D., Wilson, R.J.: Observation of atomic corrugation on Au (111) by scanning tunneling microscopy. Phys. Rev. Lett. **59**, 2879 (1987)
13. Schmid, M., Stadler, H., Varga, P.: Direct observation of surface chemical order by scanning tunnelling microscopy. Phys. Rev. Lett. **70**, 1441 (1993)
14. Hebenstreit, E.L.D., Hebenstreit, W., Schmid, M., Varga, P.: $Pt_{25}Rh_{75}$(111), (110) and (100) studied by scanning tunnelling microscopy with chemical contrast. Surf. Sci. **441**, 441 (1999)
15. Wouda, P.T., Schmid, M., Nieuwenhuys, B.E., Varga, P.: STM study of the (111) and (100) surface of AgPd. Surf. Sci. **417**, 292 (1998)
16. Gauthier, Y., Baudoing-Savois, R., Bugnard, J.M., Hebenstreit, W., Schmid, M., Varga, P.: Segregation and chemical ordering in the surface layers of $Pd_{25}Co_{75}$(111): a LEED/STM study. Surf. Sci. **466**, 155 (2000)
17. Ondracek, M., Maca, F., Kudrnovsky, J., Redinger, J., Biedermann, A., Fritscher, C., Schmid, M., Varga, P.: Chemical ordering and composition fluctuations on the (001) surface of the $Fe_{64}Ni_{36}$ invar alloy. Phys. Rev. B **74**, 235437 (2006)
18. Murray, P.W., Stesgaard, I., Laegsgaard, E., Besenbacher, F.: Growth and structure of Pd alloys on Cu(100). Surf. Sci. **365**, 591 (1996)
19. Hoster, H.E., Filonenko, E., Richter, B., Behm, R.J.: Formation and short-range order of two-dimensional $Cu_xPd_{1-x}$ monolayer surface alloys on Ru(0001). Phys. Rev. B **73**, 165413 (2006)
20. Hebenstreit, W., Schmid, M., Redinger, J., Podloucky, R., Varga, P.: Bulk terminated NaCl(111) on aluminum: a polar surface of a ionic crystal? Phys. Rev. Lett. **85**, 5376 (2000)
21. Schintke, S., Schneider, W.-D.: Insulators at the ultrathin limit: electronic structure studied by scanning tunnelling microscopy and scanning tunnelling spectroscopy. J. Phys. Condens. Matter **16**, R49 (2004)
22. Kresse, G., Schmid, M., Napetshnig, A., Shishkin, M., Köhler, L., Varga, P.: Structure of ultrathin aluminum oxide film on NiAl(110). Science **308**, 1440 (2005)
23. Wintterlin, J., Völkening, S., Janssens, T.U.V., Zambelli, T., Ertl, G.: Atomic and macroscopic reaction rates of a surface-catalyzed reaction. Science **278**, 1931 (1997)
24. Stipe, B.C., Razaei, M.A., Ho, W.: Single-molecule vibrational spectroscopy and microscopy. Science **280**, 1732 (1998)
25. Eigler, D.M., Schweizer, E.K.: Positioning single atoms with a scanning tunnelling microscope. Nature **344**, 524 (1990)
26. Hahn, J.R., Ho, W.: Single-molecule imaging and vibrational spectroscopy with a chemically modified tip of scanning tunnelling microscope. Phys. Rev. Lett. **87**, 196102 (2001)
27. Nilius, N., Wallis, T.M., Ho, W.: Building alloys from single atoms: Au-Pd chains on NiAl(110). J. Phys. Chem. B **108**, 14616 (2004)

28. Hla, S.W., Bartels, L., Meyer, G., Rieder, K.H.: Inducing all steps of a chemical reaction with the scanning tunneling microscope tip: toward single molecule engineering. Phys. Rev. Lett. **85**, 2777 (2000)
29. Katano, S., Kim, Y., Hori, M., Trenary, M., Kawai, M.: Reversible control of hydrogenation of a single molecule. Science **316**, 1883 (2007)
30. Binnig, G., Quate, C.F., Gerber, Ch.: Atomic force microscope. Phys. Rev. Lett. **56**, 930 (1986)
31. Morita, S., Wiesendanger, R., Meyer, E.: Noncontact Atomic Force Microscopy. Springer, Berlin (2002)
32. Meyer, E., Hug, H.-J., Bennewitz, R.: Scanning Probe Microscopy: The Lab on a Tip. Springer, Berlin (2004)
33. Shluger, A.L., Livshits, A.I., Foster, A.S., Catlow, C.R.A.: Models of image contrast in scanning force microscopy on insulators. J. Phys. Condens. Matter **11**, R295 (1999)
34. Howald, L., Haefke, H., Lüthi, R., Meyer, E., Gerth, G., Rudin, H., Güntherodt, H.-J.: Ultra-high vacuum scanning force microscopy: atomic-scale resolution at monoatomic cleavage steps. Phys. Rev. B **49**, 5651 (1994)
35. Albrecht, T.R., Grütter, P., Horne, D., Rugar, D.: Frequency modulation detection using high-Q-cantilevers for enhanced force microscope sensitivity. J. Appl. Phys. **69**, 668 (1991)
36. Oyabu, N., Custance, Ó., Yi, I., Sugawara, Y., Morita, S.: Mechanical vertical manipulation of selected single atoms by soft nanoindentation using near contact atomic force microscopy. Phys. Rev. Lett. **90**, 176102 (2003)
37. Giessibl, F.J.: Atomic resolution of the silicon (111)−(7×7) surface by atomic force microscopy. Science **267**, 68 (1995)
38. Giessibl, F.J.: Advances in atomic force microscopy. Rev. Mod. Phys. **75**, 949 (2003)
39. Bonnell, D.A., Garra, J.: Scanning probe microscopy of oxide surfaces: atomic structure and properties. Rep. Prog. Phys. **71**, 044501 (2008)
40. Lauritsen, J.V., Reichling, M.: Atomic resolution non-contact atomic force microscopy of clean metal oxide surfaces. J. Phys. Condens. Matter **22**, 263001 (2010)
41. Barth, C., Foster, A.S., Henry, C., Shluger, A.L.: Recent trends in surface characterization and chemistry with high-resolution scanning force methods. Adv. Mater. **23**, 477 (2011)
42. Sugimoto, Y., Pou, P., Abe, M., Jelinek, P., Pérez, R., Morita, S., Custance, Ó.: Chemical identification of individual surface atoms by atomic force microscopy. Nature **446**, 64 (2007)
43. Sugimoto, Y., Pou, P., Custance, Ó., Jelinek, P., Morita, S., Pérez, R., Abe, M.: Real topography, atomic relaxations, and short-range chemical interactions in atomic force microscopy: the case of the α-Sn/Si(11)-($\sqrt{3}$x$\sqrt{3}$)*R*30° surface. Phys. Rev. B **73**, 205329 (2006)
44. Barth, C., Foster, A.S., Reichling, M., Shluger, A.L.: Contrast formation in atomic resolution scanning force microscopy on $CaF_2$(111): experiment and theory. J. Phys. Condens. Matter **13**, 2061 (2001)
45. Barth, C., Henry, C.: Imaging Suzuki precipitates on NaCl:$Mg^{2+}$(001) by scanning force microscopy. Phys. Rev. Lett. **100**, 096101 (2008)
46. Henry, C.: Morphology of supported nanoparticles. Prog. Surf. Sci. **80**, 92 (2005)
47. Perrot, E., Humbert, A., Piednoir, A., Chapon, C., Henry, C.: STM and TEM studies of a model catalyst: Pd/$MoS_2$(0001). Surf. Sci. **445**, 407 (2000)
48. Hansen, K.H., Worren, T., Stempel, S., Lægsgaard, E., Bäumer, M., Freund, H.-J., Besenbacher, F., Stensgaard, I.: Palladium nanocrystals on Al2O3: structure and adhesion energy. Phys. Rev. Lett. **83**, 4120 (1999)
49. Dulub, O., Hebenstreit, W., Diebold, U.: Imaging cluster surfaces with atomic resolution: the strong metal-support interaction state on Pt supported on $TiO_2$(110). Phys. Rev. Lett. **84**, 3646 (2000)
50. Silly, F., Castell, M.R.: Selecting the shape of supported metal nanocrystals: Pd huts, hexagons or pyramids on $SrTiO_3$(001). Phys. Rev. Lett. **94**, 046103 (2005)
51. Piednoir, A., Perrot, E., Granjeaud, S., Humbert, A., Chapon, C., Henry, C.: Atomic resolution on small 3D metal clusters by STM. Surf. Sci. **391**, 19 (1997)

52. Dai, H., Hafner, J.H., Rinzler, A.G., Colbert, D.T., Smalley, R.: Nanotubes as nanoprobes in scanning probe microscopy. Nature **384**, 147 (1996)
53. Ferrero, S., Piednoir, A., Henry, C.: Atomic scale imaging by UHV-AFM of nanosized gold particles on mica. Nano Lett. **1**, 227 (2001)
54. Højrup-Hansen, K., Ferrero, S., Henry, C.: Nucleation and Growth kinetics of gold nanoparticles on MgO(100) studied by UHV-AFM. Appl. Surf. Sci. **226**, 167 (2004)
55. Barth, C., Henry, C.: High resolution imaging of gold clusters on KBr(100) surfaces investigated by dynamic scanning force microscopy. Nanotechnology **15**, 1264 (2004)
56. Szymonski, M., Goryl, M., Krok, F., Kolodziej, J.J., de Mongeot, F.B.: Metal nanostructures assembled at semiconductor surfaces studied with high resolution scanning probes. Nanotechnology **18**, 044016 (2007)
57. Pakarinen, O.H., Barth, C., Foster, A.S., Henry, C.: High resolution scanning force microscopy of gold nanoclusters on the KBr(001) surface. Phys. Rev. B **73**, 235428 (2006)
58. Fain, Jr, S.C., Polwarth, C.A., Tait, S.L., Campbell, C.T., French, R.H.: Simulated measurement of small metal clusters by frequency-modulation non-contact atomic force microscopy. Nanotechnology **17**, S121 (2006)
59. Barth, C., Pakarinen, O.H., Foster, A.S., Henry, C.: Imaging nanoclusters in the constant height mode of the dynamic SFM. Nanotechnology **17**, S128 (2006)
60. Pakarinen, O.H., Barth, C., Foster, A.S., Henry, C.: Imaging the real shape of nanoclusters in scanning force microscopy. J. Appl. Phys. **103**, 054313 (2008)
61. Hill, I.G., Rajagopal, A., Kahn, A., Hu, Y.: Molecular level alignment at organic semiconductor-metal interfaces. Appl. Phys. Lett. **73**, 662 (1998)
62. Giordano, L., Cinquini, F., Pacchioni, G.: Tuning the surface metal work function by deposition of ultrathin oxide films: density functional calculations. Phys. Rev. B **73**, 045414 (2005)
63. Zhang, C., Yoon, B., Landman, U.: Predicted oxidation of CO catalyzed by Au nanoclusters on a thin defect-free MgO film supported on a Mo(100) surface. J. Amer. Chem. Soc. **129**, 2228 (2007)
64. Gross, L., Mohn, F., Liljeroth, P., Repp, J., Giessibl, F.J., Meyer, G.: Measuring the charge state of an adatom with noncontact atomic force microscopy. Science **324**, 1428 (2009)
65. Girard, P.: Electrostatic force microscopy: principles and some applications to semiconductors. Nanotechnology **12**, 485 (2001)
66. Berger, R., Butt, H.J., Retschke, M.B., Weber, S.A.L.: Electrical modes in scanning probe microscopy. Macromol. Rapid Commun. **30**, 1167 (2009)
67. Palermo, V., Palma, M., Samori, P.: Electronic characterization of organic thin films by kelvin probe force microscopy. Adv. Mater. **18**, 145 (2006)
68. Melitz, W., Shen, J., Kummel, A.C., Lee, S.: Kelvin probe force microscopy and its application. Surf. Sci. Rep. **66**, 1 (2011)
69. Weaver, J.M.R., Abraham, D.W.: High resolution atomic force microscopy potentiometry. J. Vac. Sci. Technol. B **9**, 1559 (1991)
70. Nonnenmacher, M., O'Boyle, M.P., Wickramasinghe, H.K.: Kelvin probe force microscopy. Appl. Phys. Lett. **58**, 2921 (1991)
71. Barth, C., Henry, C.: Kelvin probe force microscopy on surfaces of UHV-cleaved ionic crystals. Nanotechnology **17**, S155 (2006)
72. Barth, C., Henry, C.: Surface double layer on (001) surfaces of alkali halide crystals: a scanning force microscopy study. Phys. Rev. Lett. **98**, 136804 (2007)
73. Henry, C.: Surface studies of supported model catalysts. Surf. Sci. Rep. **31**, 235 (1998)
74. Heiz, U., Landman, U. (eds.): Nanocatalysis. Springer, Berlin (2007)
75. Glatzel, T., Sadewasser, S., Lux-Steiner, M.C.: Amplitude or frequency modulation-detection in Kelvin probe force microscopy. Appl. Surf. Sci. **210**, 84 (2003)
76. Kitamura, S., Iwatsuki, M.: High-resolution imaging of contact potential difference with ultra high vacuum noncontact atomic force microscope. Appl. Phys. Lett. **72**, 3154 (1998)

77. Krok, F., Sajewicz, K., Konior, K., Goryl, M., Piatkowski, P., Szymonski, M.: Lateral resolution and potential sensitivity in the Kelvin probe force microscopy: towards understanding of the sub-nanometer resolution. Phys. Rev. B **77**, 235427 (2008)
78. Barth, C., Henry, C.: Gold nanoclusters on alkali halide surfaces: charging and tunnelling. Appl. Phys. Lett. **89**, 252119 (2006)
79. Sasahara, A., Pang, C.L., Onishi, H.: Local work function of Pt clusters vacuum-deposited on a $TiO_2$ surface. J. Phys. Chem. B **110**, 17584 (2006)
80. Barth, C., Henry, C.: Kelvin force microcopy on MgO(001) surfaces and supported nanoclusters. J. Phys. Chem. C **113**, 247 (2009)
81. Sasahara, A., Pang, C.L., Onishi, H.: Probe microscope observation of platinum atoms deposited on the $TiO_2$(110)-(1x1) surface. J. Phys. Chem. B **110**, 13453 (2006)
82. Bieletzki, M., Hynninen, T., Soini, T.M., Pivetta, M., Henry, C., Foster, A.S., Esch, F., Barth, C., Heiz, U.: Topography and work function measurements of thin MgO(001) films on Ag(001) by nc-AFM and KPFM. Phys. Chem. Chem. Phys. **12**, 3203 (2010)
83. Niedermayer, R., Mayer, R.: Basic problems in thin film physics. Vandenhoeck & Ruprecht, Göttingen (1966)
84. Mathews, J.W.: Epitaxial Growth Part B. Academic press, New York (1975)
85. Kern, R., Lelay, G., Métois, J.J.: Basic mechanisms in the early stages of epitaxy. In: Kaldis, E. (ed.) Current Topics in Materials Science, vol. 3, p. 131. North Holland, Amsterdam (1979)
86. Volmer, M.: Kinetic der Phasenbildung. T. Steinkopff Verlag, Leipzig (1939)
87. Zinsmeister, G.: A contribution to Frenkel's theory of condensation. Vacuum **16**, 529 (1966)
88. Frenkel, J.: Theorie der adsorption und verwandter erscheinungen. Z. Physik **26**, 117 (1924)
89. Robins, J.L., Rhodin, T.N.: Nucleation of metal crystals on ionic surfaces. Surf. Sci. **2**, 346 (1964)
90. Henry, C.: Growth, structure and morphology of supported metal clusters studied by surface science techniques. Cryst. Res. Technol. **33,** 1119 (1998)
91. Meunier, M., Henry, C.: Nucleation and growth of metallic clusters on MgO(100) by helium diffraction. Surf. Sci. **307**, 514 (1994)
92. Gimenez, F., Chapon, C., Henry, C.: Nucleation and growth kinetics of Pd and CuPd particles on NaCl(100). New J. Chem. **22**, 1289 (1998)
93. Haas, G., et al.: Nucleation and growth of supported clusters at defect sites: Pd/MgO(001). Phys. Rev. B **61**, 11105 (2000)
94. Venables, J.A., Harding, J.H.: Nucleation and growth of supported metal clusters at defect sites on oxide and halide (001) surfaces. J. Cryst. Growth **211**, 27 (2000)
95. Zinsmeister, G.: Theory of thin film condensation part C: aggregates size distribution in island films. Thin Solid Films **4**, 363 (1969)
96. Halpern, V.: Cluster growth and saturation island densities in thin film growth. J. Appl. Phys. **40**, 4627 (1969)
97. Sigsbee, R.A.: Adatom capture and growth rates of nuclei. J. Appl. Phys. **42**, 3904 (1971)
98. Stowell, M.J.: Capture numbers in thin film nucleation theories. Phil. Mag. **26**, 349 (1972)
99. Lewis, B.: Migration and capture processes in heterogeneous nucleation and growth I. Theory Surf. Sci. **21**, 273 (1970)
100. Venables, J.A.: Rate equation approaches to thin film nucleation kinetics. Phil. Mag. **27**, 697 (1973)
101. Lewis, B., Rees, G.: Adatom migration, capture and decay among competing nuclei on a susbtrate. Phil. Mag. **29**, 1253 (1974)
102. Kashchiev, D.: Mean thickness at which vapour-deposited thin films reach continuity. Thin Solid Films **55**, 399 (1978)
103. Kashchiev, D.: Growth of crystallites in deposition from vapours. Phys. Status Solidi (a) **64**, 715 (1981)
104. Henry, C., Meunier M.: Power laws in the growth kinetics of metal clusters on oxide surfaces. Vacuum **50**, 157 (1998)

105. Rosenhahn, A., Schneider, J., Becker, C., Wandelt, K.: Oxidation of $Ni_3Al(111)$ at 600, 800 and 1050 K investigated by scanning tunnelling microscopy. J. Vac. Sci. Technol. A **18**, 7 (2000)
106. Hamm, G., Barth, C., Becker, C., Wandelt, K., Henry, C.: Power laws in the growth kinetics of metal clusters on oxide surfaces. Phys. Rev. Lett. **97**, 126106 (2006)
107. Schmid, M., Kresse, G., Buchsbaum, A., Napetschning, E., Gritschneder, S., Reichling, M., Varga, P.: Nanotemplate with holes: Ultrathin alumina on $Ni_3Al(111)$. Phys. Rev. Lett. **99**, 196104 (2007)
108. Sedona, F., Granozzi, G., Barcaro, G., Fortunelli, A.: Defect evolution in oxide nanophases: the case of a zigzag- like $TiO_x$ phase on Pt(111). Phys. Rev. B **77**, 115417 (2008)
109. Torelli, P., Soares, E.A., Renaud, G., Gragnaniello, L., Valeri, S., Guo, X.X., Luches, P.: Self-organized growth of Ni nanoparticles on a cobalt-oxide thin film induced by a buried misfit dislocation network. Phys. Rev. B **77**, 081409 (2008)
110. Becker, C., Rosenhahn, A., Wiltner, A., von Bergmann, K., Schneider, J., Pervan, P., Milun, M., Kralj, M., Wandelt, K.: $Al_2O_3$-films on $Ni_3Al(111)$: a template for nanostructured cluster growth. New J. Phys. **4**, 75 (2002)
111. Hamm, G., Becker, C., Henry, C.: Pd-Au nanocluster arrays grown on nanostructured alumina templates. Nanotechnology **17**, 1943 (2006)
112. Barcaro, G., Fortunelli, A., Granozzi, G., Sedona, F.: Cooperative phase transformation in self-assembled metal-on-oxide arrays. J. Phys. Chem. C **113**, 1143 (2009)
113. Rohart, S., Baudot, G., Repain, V., Girard, Y., Rousset, S., Bulou, H., Goyhenex, C., Proville, L.: Atomistic mechanisms for the ordered growth of Co nanodots on Au(788): a comparison between VT-STM experiments and multiscaled calculations. Surf. Sci. **559**, 47 (2004)
114. Sitja, G., Unac, R.O., Henry, C.: Kinetic Monte Carlo simulation of the growth of metal clusters on a regular array of defects on the surface of an insulator. Surf. Sci. **604**, 404 (2010)
115. Anton, R., Harsdorff, M.: Extension of the kinetic nucleation model to binary alloys. Thin Solid Films **44**, 341 (1977)
116. Anton, R., Harsdorff, M., Martens, T.H.: Nucleation and growth of binary alloys on substrates. Thin Solid Films **57**, 233 (1979)
117. Anton, R., Dröske, R.: Nucleation of Au-Ag binary alloys from the vapour on KBr single crystals. Thin Solid Films **124**, 155 (1985)
118. Kortekamp, T., Anton, R., Harsdorff, M.: Nucleation and growth of Au-Cu binary alloys from the vapour phase on NaCl single crystals. Thin Solid Films **145**, 123 (1986)
119. Anton, R., Schmidt, A., Schünemann, V.: Heterogeneous nucleation of binary alloy particles. Vacuum **41**, 1099 (1990)
120. Schmidt, A., Schünemann, V., Anton, R.: Monte Carlo simulation of the nucleation of binary-alloys particles of Au, Ag and Pd on NaCl substrates. Phys. Rev. B **41**, 11875 (1990)
121. Schmidt, A., Spode, M., Heinrich, J., Anton, R.: The nucleation and growth of Pd-Au alloy particles on NaCl(100). Thin Solid Films **196**, 253 (1991)
122. Alloyeau, D., Prévot, G., Le Bouar, Y., Oikawa, T., Langlois, C., Loiseau, A., Ricolleau, C.: Ostwald ripening in nanoalloys: when thermodynamics drives a size-dependent particle composition. Phys. Rev. Lett. **105**, 255901 (2010)
123. Herzing, A.A., Watanabe, M., Edwards, J.K., Conte, M., Tang, Z.R., Hutchnings, G.J., Kiely, C.J.: Energy dispersive X-ray spectroscopy of bimetallic nanoparticles in an aberration corrected scanning transmission electron microscope. Faraday Discuss. **138**, 337 (2008)
124. Gimenez, F., Chapon, C., Giorgio, S., Henry, C.: Bimetallic Pd-Cu clusters particles supported on NaCl. In: Proceedings ICEM 13, Paris, p. 351 (1994)
125. Gimenez, F.: Nucléation, croissance, composition et structure d'agrégats bimétalliques suopportés. Ph.D. thesis, Marseille (1997)
126. Gai, Z., Howe, J.Y., Guo, J., Blom, D.A., Plummer, E.W., Shen, J.: Self-assembled FePt nanodots arrays with mono-dispersion and -orientation. Appl. Phys. Lett. **86**, 023107 (2005)

127. Gross, E., Popov, I., Ascher, M.: Chemical reactivity of Pd-Au bimetallic nanoclusters grown via amorphous solid water as buffer layer. J. Phys. Chem. C **113**, 18341 (2009)
128. Abbott, H.I., Aumer, A., Lei, Y., Asokan, C., Meyer, R.J., Sterrer, M., Shaikhutdinov, S., Freund, H.-J.: CO adsorption on monometallic and bimetallic Au-Pd nanoparticles supported on oxide thin films. J. Phys. Chem. C **114**, 17099 (2010)
129. Heemeier, M., Carlsson, A.F., Naschitzki, M., Schmal, M., Bäumer, M., Freund, H.-J.: Preparation and characterization of a model bimetallic catalyst: Co-Pd nanoparticles supported on $Al_2O_3$. Angew. Chem. Int. Ed. **41**, 4073 (2002)
130. Carlsson, A.F., Naschitzki, M., Bäumer, M., Freund, H.-J.: The structure and reactivity of $Al_2O_3$-supported cobalt-palladium particles: a CO-TPD, STM and XPS study. J. Phys. Chem. B **107**, 778 (2003)
131. Carlsson, A.F., Bäumer, M., Risse, T., Freund, H.-J.: Surface structure of Co-Pd bimetallic particles supported on $Al_2O_3$ thin films studied using infrared reflection absorption spectroscopy of CO. J. Chem. Phys. **119**, 10885 (2003)
132. Napetschnig, E., Schmid, M., Varga, P.: Pd, Co and Co-Pd clusters on the ordered alumina film on NiAl(110). Contact angle, surface structure and composition. Surf. Sci. **601**, 3233 (2007)
133. Felicissimo, M.P., Martyanov, O.N., Risse, T., Freund, H.-J.: Characterization of Pd-Fe bimetallic model catalysts. Surf. Sci. **601**, 2105 (2007)
134. Han, P., Goodman, D.W.: Controlling the size and distribution of Pd-Au nanoparticles on $TiO_2$(110). J. Phys. Chem. C **112**, 6390 (2008)
135. Khan, N.A., Uhl, A., Shaikhutdinov, S., Freund, H.-J.: Alumina supported model Pd-Ag catalysts: a combined STM, XPS, TPD and IRAS study. Surf. Sci. **600**, 1849 (2006)
136. Marsault, M., Hamm, G., Wörz, A., Sitja, G., Barth, C., Henry, C.: Preparation of regular arrays of bimetallic clusters with independent control of size and chemical composition. Faraday Discuss **138**, 407 (2008)
137. Santra, A.K., Yang, F., Goodman, D.W.: The growth of Ag-Au bimetallic nanoparticles on $TiO_2$(110). Surf. Sci. **548**, 324 (2004)
138. Bassett, G.A.: A new technique for decoration of cleavage and slip steps on ionic crystal surfaces. Phil. Mag. **3**, 1042 (1958)
139. Park, J.B., Ratliff, J.S., Ma, S., Chen, D.A.: In situ scanning tunneling microscopy studies of bimettalic cluster growth: Pt-Rh on TiO2(110). Surf. Sci. **600**, 2913 (2006)
140. Marsault M.: Réseaux réguliers d'agrégats mono et bimétalliques sur des substrats d'alumine nanostructurée. Ph.D. thesis, Marseille (2010)
141. Degen, S., Becker, C., Wandelt, K.: Thin alumina films on $Ni_3Al$(111): a template for nanostructured Pd clusters growth. Faraday Discuss. **125**, 343 (2003)
142. Krawczyk, M., Zommer, L., Lesiak, B., Jablonski, A.: Surface composition of the CoPd alloys studied by electron spectroscopies. Surf. Interface Anal. **25**, 356 (1997)
143. Diebold, U., Pan, J.M., Madey, T.E.: Growth mode of of ultrathin copper overlays on $TiO_2$(1101). Phys. Rev. B **47**, 3868 (1993)
144. Luo, K., Wei, T., Yi, C.W., Axnanda, S., Goodman, D.W.: Preparation and characterization of silica supported Au-Pd model catalysts. J. Phys. Chem. B **109**, 23517 (2005)
145. Gustafson, J., Haire, A.R., Baddeley, C.: Depth-profiling the composition of bimetallic nanoparticles using medium energy ion scattering. Surf. Sci. **605**, 220 (2011)
146. Haire, A.R., Gustafson, J., Trant, A.G., Jones, T.E., Noakes, T.C.Q., Bailey, P., Baddeley, C.J.: Influence of preparation conditions on the depth-dependent composition of AuPd nanoparticles grown on planar oxide surfaces. Surf. Sci. **605**, 214 (2011)
147. Bradeley, J.S., Hill, E.W., Chaudret, B., Duteil, A.: Surface chemistry on colloidal metals. Reversible adsorbate-induced surface composition changes in colloidal palladium-copper alloys. Langmuir **11**, 693 (1995)
148. Gao, F., Wang, Y., Goodman, D.W.: Reaction kinetics and polarization-modulation infrared reflection absorption spectroscopy (PM-IRAS) investigation of CO oxidation over supported Pd-Au alloy catalysts. J. Phys. Chem. C **114**, 4036 (2010)

149. Vitos, L., Ruban, A.V., Skriver, H.L., Kollar, J.: The surface energy of metals. Surf. Sci. **411**, 186 (1998)
150. Gross, L., Mohn, F., Moll, N., Liljeroth, P., Meyer, G.: The chemical structure of a molecule resolved by atomic force microscopy. Science **325**, 1110 (2009)
151. Langlois, C., Alloyeau, D., Le Bouar, Y., Loiseau, A., Oikawa, T., Mottet, C., Ricolleau, C.: Growth and structural properties of CuAg and CoPt bimetallic nanoparticles. Faraday Discuss. **138**, 375 (2008)
152. Goryl, M., Krok, F., Kolodziej, J.J., Piatkowski, P., Such, B., Szymonski, M.: Surface structure of Au/InSb(001) system investigated with scanning force microscopy. Vacuum **74**, 223 (2004)
153. Renaud, G., Lazzari, R., Revenant, C., Barbier, A., Noblet, M., Ullrich, O., Leroy, F., Borensztein, Y., Jupille, J., Henry, C., Deville, J.P., Scheurer, F., Mane–Mane, J., Fruchart, O.: In situ GISAXS towards a real time modelling of growing nanoparticles. Science **300**, 1416 (2003)
154. Benten, W., Nilius, N., Ernst, N., Freund, H.-J.: Photon emission spectroscopy of single oxide-supported Ag-Au alloy clusters. Phys. Rev. B **72**, 045403 (2005)

http://www.springer.com/978-1-4471-4013-9

Nanoalloys
Synthesis, Structure and Properties
Alloyeau, D.; Mottet, C.; Ricolleau, C. (Eds.)
2012, VIII, 412 p., Hardcover
ISBN: 978-1-4471-4013-9